LRP1 endocytosis is regulated by KIF13B through the interaction with hDLG1

A thesis submitted by

Joslyn E. Mills

in partial fulfillment of the requirements for the degree of

Doctor of Philosophy

In

Cellular and Molecular Physiology

Tufts University

Sackler School of Graduate Biomedical Sciences

May 2018

Advisors: Laura Liscum, PhD and Athar Chishti, PhD

Abstract

KIF13B, a kinesin-3 family motor, was originally identified by virtue of its biochemical interaction with human homolog of *Drosophila* discs large tumor suppressor (hDLG1). Unlike its homolog KIF13A, the KIF13B contains a carboxyl-terminal CAP-Gly domain. To investigate the specific functional role of the CAP-Gly domain in KIF13B, and its possible compensation by KIF13A, we developed two mouse models. One mouse model expresses a truncated form of KIF13B protein lacking only its CAP-Gly domain (KIF13BΔCG), whereas the second model lacks the full-length KIF13A (KIF13A FLKO). Using these mouse models, we show that the KIF13BΔCG mice exhibit relatively higher levels of serum cholesterol consistent with the reduced uptake of [^{3}H]CO-LDL in KIF13BΔCG mouse embryo fibroblasts. In contrast, the serum level of factor VIII was not significantly elevated in the KIF13BΔCG as compared to wild-type mice, suggesting that the CAP-Gly domain of KIF13B selectively regulates Low density lipoprotein Related Protein 1-mediated lipoprotein endocytosis. No elevation of either serum cholesterol or factor VIII was observed in the KIF13A FLKO. Moreover, we found that the deletion of the CAP-Gly domain caused subcellular mislocalization of truncated KIF13B with concomitant mislocalization of LRP1. To further delineate the biochemical basis of the LRP1-KIF13B complex at the plasma membrane, we discovered that the cytoplasmic domain of LRP1 interacts specifically with the alternatively spliced I_3 domain of hDLG1, which in turn recognizes the MBS domain of KIF13B. Together, this study provides evidence for the biochemical basis of LRP1-hDlg1-KIF13B complex formation, which regulates LRP1-mediated interactions with implications in metabolism, cell polarity, and development.

Dedication

To my family, making you proud was a driving force for my hard work and dedication to the scientific field.

To my friends, with whose little help I get by.

And especially **to Dennis**, who deserves his own degree for the support he has given me while I pursue mine, and beyond.

Acknowledgements

First, I want to thank my co-mentors, Dr. Laura Liscum and Dr. Athar Chishti for their immeasurable support and confidence in me. Laura has supported me from the beginning through all the ups and downs, and we finally made it to the end! In addition to supporting my research, there is no one better than her to prepare me for a career in teaching. Athar was my champion for taking me into his lab late in the game. Without him, I would not have a body of work that is so worthy of defending.

Next, I want to thank my committee members, Dr. Brent Cochran and Dr. Peter Juo, for their insightful advice and guidance; Brent, for his patience in helping me through all my different projects, and Peter, for taking over as my chair for this final project.

I also want to thank Dr. Jerry Faust, my original committee chair. In addition to the important scientific conversations we had, I am grateful for him knowing when I needed to chat about something else to forget about my frustration with my projects for a while.

I want to thank Dr. Toshi Hanada for laying the groundwork for this project and sharing it with me, and I only hope I have done it justice.

Additionally, I want to thank the support staff, Andrea Flaherty, Elaine Ross, Jeanne Rose, Karen Hatch, and Di Pierce, for making it feel like you are all my own personal support group. Your friendships mean the world to me, and I am so grateful I had you all to get though the tough times as well as the happy times.

Finally, thank you to all that contributed to the manuscript and foundation of this project: Yunzhe Lu, Yoichi Hase, Janis Lem, Lauren Richie, Bina Julian, Madhumouli Chatterjee from Dr. Gary Gilbert's lab, Dr. Joachim Herz and Rebekah Hewitt, Dr. Alice Lichtenstein and HNRC Nutrition Evaluation Lab: Gayle Petty and Stephanie Thea Leon Valliere, TUSM histology core: Nathan Li, Tufts University Core Facility, and Dr. Roderick Bronson from HSM.

Table of Contents

List of Figures

List of Copyrighted Materials

Hirokawa N, Noda Y, Tanaka Y, Niwa S. Kinesin superfamily motor proteins and intracellular transport. Nat Rev Mol Cell Biol. 2009;10(10):682-96. doi: 10.1038/nrm2774.

Kanai Y, Wang D, Hirokawa N. KIF13B enhances the endocytosis of LRP1 by recruiting LRP1 to caveolae. The Journal of cell biology. 2014;204(3):395-408. doi: 10.1083/jcb.201309066.

List of Abbreviations

CAP-Gly (Cytoskeleton-Associated Protein Glycine-rich)
CG (CAP-Gly)
DKO (double “knock out”)
FHA (forkhead associated)
FLKO (full-length knock out)
hDLG1 (human discs large tumor suppressor 1)
GAKIN (guanylate kinase associated kinesin)
GUK (guanylate kinase-like)
LDL (low density lipoprotein)
LDLr (low density lipoprotein receptor)
LPDS (lipoprotein-deficient serum)
LRP1 (LDL-receptor Related Protein 1)
MAGUK (membrane-associate guanylate kinase)
MEFs (mouse embryonic fibroblasts)
SH3 (Src homology 3)

Chapter 1: INTRODUCTION

1.1 Kinesin motor proteins

The kinesin superfamily of motor proteins, or KIFs, are motor proteins that transport various cargos through the cell along microtubules. As shown in Figure 1.1 (1), KIFs are very diverse, with 15 families of kinesins that can be categorized into three groups based on the orientation of their motor domain, the N-, C-, and M-kinesins. The motor domain of N-kinesins is located at the N-terminus of the protein, and they transport cargo toward the plus end of microtubules, typically in an anterograde (toward the plasma membrane) direction. In contrast, a C-kinesin's motor domain is located at the C-terminus of the protein, and they transport cargo toward the minus end of microtubules, usually in a retrograde direction, similar to dynein. Finally, the motor domain of M-kinesins is located in the center of the protein, and these kinesins depolymerize microtubules. The diversity of KIFs allows for the recognition of different binding proteins, thus allowing for transport of diverse cargos, such as vesicles containing protein complexes and mRNA, whole organelles, and lipids (Figure 1.1B). KIFs typically exist as homodimers, which allows the protein to "walk" along microtubules through an ATP hydrolysis reaction, with the exception of KIF1A and KIF1B, which are monomers that "hop" along the track (1).

1.1.1 KIF13 Family

The KIF13 motor proteins are N-kinesins in the Kinesin 3 family. Structurally, KIF13A and KIF13B are very similar; however, they play very different roles. KIF13A interacts with the AP1 binding complex to transport vesicles containing mannose-6-

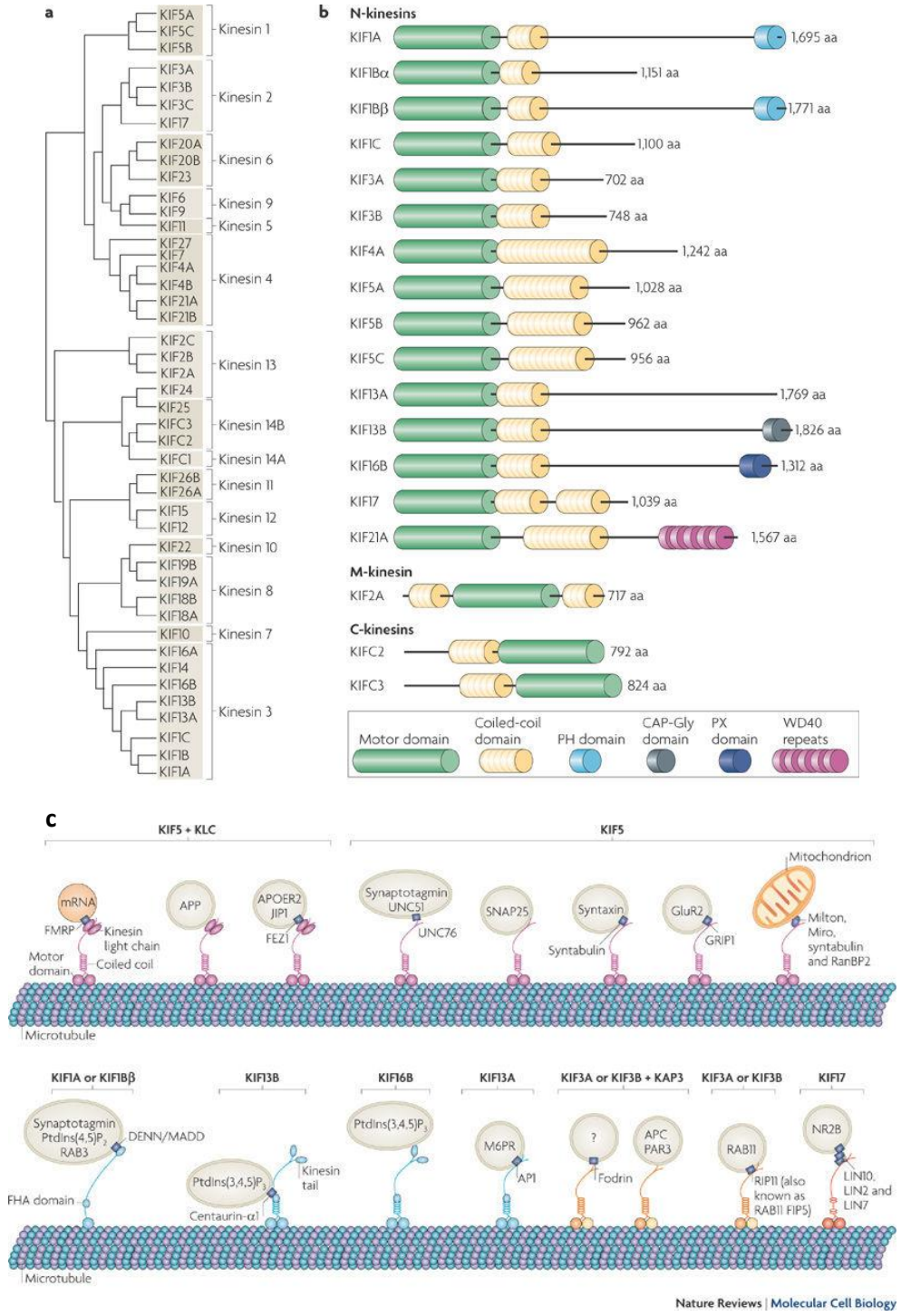

Figure 1.1. Kinesin super family. A) A phylogenetic tree of all 45 KIF genes in the mouse genome, which are classified into 15 families. B) The domain structure of the major kinesins. The 15 families of kinesins can be broadly grouped into N-kinesins, M-kinesins and C-kinesins, which contain their motor domain at the amino terminus, in the middle or at the carboxyl terminus, respectively. KIF13B is the only known KIF with a CAP-Gly domain. C) KIF cargo is very diverse. Kinesins associate with microtubules through

(Figure 1.1. continued from page 2) their head motor domains, either as monomers (one sphere) or dimers (two spheres). KIFs associate with their indicated cargos through their tails or occasionally through their light chains or adaptor or scaffold proteins. AP1, adaptor protein complex 1; APC, adenomatous polyposis coli; APP, β-Amyloid precursor protein; FEZ1, fasciculation and elongation protein- ζ1; FHA, Forkhead associated; FMRP, fragile X mental retardation protein (also known as FMR1); GluR2, AMPA (α-amino-3-hydroxy-5-methyl-4-isoxazole propionic acid)-type glutamate receptor 2; GRIP1, glutamate receptor-interacting protein 1; JIP1, JUN amino-terminal kinase (JNK)-interacting protein 1 (also known as MAPK8IP1); KAP3, kinesin superfamily-associated protein 3 (also known as KIFAP3); M6PR, mannose-6-phosphate receptor, cation dependent;NR2B, NMDA (N-methyl-D-aspartate)-type glutamate receptor 2B; PAR3, partitioning defective 3; PtdIns(3,4,5)P_3, phosphatidylinositol3,4,5-trisphosphate; PtdIns(4,5)P_2, phosphatidylinositol 4,5-bisphosphate; RanBP2, Ran-binding protein 2; RIP11, RAB11 family-interacting protein 3 (also known as RAB11FIP5); SNAP25, soluble N-ethylmaleimide-sensitive factor attachment protein 25. Reprinted with permission from Hirokawa N, Noda Y, Tanaka Y, Niwa S. Kinesin superfamily motor proteins and intracellular transport. Nat Rev Mol Cell Biol. 2009;10(10):682-96. doi: 10.1038/nrm2774.

phosphate receptor from the trans-Golgi network to the plasma membrane (2). KIF13A also is responsible for delivering important enzymes from recycling endosomes to nascent melanosomes during melanosome maturation (3). On the other hand, KIF13B is involved in very different transport pathways, which are discussed in detail below.

Full length KIF13B was first identified as GAKIN due to its direct binding to the guanylate kinase-like (GUK) domain of human homolog of *Drosophila* discs large tumor suppressor (hDLG1) (4). Subsequent studies revealed its similarity to KIF13A and it was thus classified as KIF13B (5). Like other Kinesin 3 family members, KIF13B has a motor domain at its N-terminus to allow its movement along the plus end of microtubules and a neck coiled-coil (NC) domain that is responsible for its transition from monomer to dimer (6). The motor activity of KIF13B is required for the transport of PIP_3-containing vesicles to regulate neuronal cell polarity (7). KIF13B also consists of other functional domains including the forkhead-associated (FHA) domain, and the MAGUK (membrane-associated GUK) Binding Stalk (MBS) domain. The FHA domain of KIF13B directly interacts with

centaurin-α_1 (also called PIP_3BP), which in turn activates ADP-ribosylation factor (ARF6) by suppressing the GAP activity of centaurin-α_1 (8). The MBS domain of KIF13B directly binds to the GUK domain of MAGUKs, such as hDLG1, and permits KIF13B-mediated transport of MAGUK-laden vesicles on microtubules (9). Direct binding of hDLG1 to the MBS domain of KIF13B activates the microtubule-stimulated ATPase activity of KIF13B, suggesting a regulatory role of this domain (10). Mammalian KIF13B shows homology to the *Drosophila* kinesin-73 motor protein, which engages its GUK domain to bind to fly Dlg1 (11, 12). KLP4, a motor protein found in *C. elegans*, is homologous to KIF13B and KIF13A, and plays a role in glutamate receptor trafficking (13).

1.1.1.1 CAP-Gly domain

The domain that distinguishes KIF13B from its homolog KIF13A is the Cytoskeleton-Associated Protein Glycine-rich (CAP-Gly) domain. This domain is a highly conserved ~80 amino acid motif located at the C-terminus of KIF13B. KIF13B is the only known kinesin with a CAP-Gly domain, and, compared to other domains, little is known about the function of this domain in KIF13B. In general, CAP-Gly domains are found in proteins targeted to the plus ends of microtubules, where they play a microtubular-based function due to its direct binding to the C-terminal EEY/F motif of microtubules (4, 14). For example, the motor protein dynein assembles with a complex called dynactin that contains $p150^{glued}$. Research has shown that the CAP-Gly domain of $p150^{glued}$ enhances the engagement of dynein onto microtubules (15), as well as having a role in other initiating steps of transport. While the CAP-Gly domain is not a direct component of the dynein protein, there may be some parallel of its function to the CAP-Gly domain of KIF13B. The limited evidence suggests that the CAP-Gly domain of KIF13B may stabilize the motor

protein by binding to a parallel microtubule or guiding its cargo to a specific destination in the cell.

The structure of CAP-Gly has been solved by crystallography (16), and its interface with microtubules or end binding protein (EB1) has been explored using magic angle spinning NMR spectroscopy (17, 18). The CAP-Gly domain contains a highly conserved GKNDG motif which has been shown to participate in the microtubule binding interface (16, 18). CAP-Gly domains have unusually high loop content and this trait is believed to confer intrinsic flexibility and allows its conformational plasticity to bind to microtubules and other proteins (18).

The CAP-Gly domains are known to regulate a variety of intracellular processes, including the dynamics of plus-end tracking proteins at the growing end of microtubules, anterograde transport of organelles/vesicles, α-tubulin detyrosination-tyrosination cycle, assembly of intra-protein switches, and tethering of microtubules to the membrane and cytoskeletal compartments (14). These diverse biochemical properties of CAP-Gly domains are consistent with their functional role in cell signaling, migration, polarity, chromosome segregation, and tumorigenesis (11, 14, 19, 20). Similarly, a critical role of CAP-Gly domains in human diseases was underscored by the identification of mutations in the $p150^{Glued}$, a subunit of dynactin, resulting in Perry syndrome and distal hereditary motor neuropathy 7B (21). Two independent mutations within the N-terminal CAP-Gly domain of $p150^{Glued}$ lead to two distinct pathologies presumably originating from the loss of dynactin binding to microtubules and CLIP-170 (22). A deletion in the CAP-Gly domain of tubulin-specific chaperone E causes a fatal disorder manifested by hypoparathyroidism, mental retardation, and facial dysmorphism (14). Additional evidence comes from the

functional inactivation of CYLD tumor suppressor that leads to benign skin and hair follicle tumors. These mutations affect the C-terminus of CYLD protein containing three CAP-Gly domains. It is believed that the disruption of the third CAP-Gly domain of CYLD likely plays a crucial role in disease pathology (23). Despite considerable evidence for their importance, the precise biological function of CAP-Gly domains remains poorly understood. One reason for this limitation is the absence of mammalian models specifically lacking the CAP-Gly domains, which will be addressed below in this thesis.

1.1.2. KIF13B and endocytosis

Recently, KIF13B has been shown to play a functional role in the uptake of lipoproteins through an LDL receptor related protein 1 (LRP1)-dependent mechanism via the FHA-MBS-CC domains of KIF13B (24). Using a full length KIF13B knock out (KIF13B FLKO) mouse model, it was shown that KIF13B can recruit LRP1 to caveolae by engaging hDLG1 as an adaptor. The KIF13B-hDLG1-LRP1 complex was further reinforced by the recruitment of utrophin and centaurin-α_1 via the CC and FHA domains, respectively, to induce LRP1 endocytosis (24). Specifically, the utrophin complex interacts with caveolin-1 in caveolae (25) and utrophin competes with caveolin for the binding to β-dystroglycan (26, 27). Additionally, the FHA domain of KIF13B binds to centaurin-α1, inhibiting its Arf6-GAP activity and activating Arf6, subsequently enhancing adjacent endocytosis (8). Due to the functional interactions of KIF13B, the motor protein offers itself as a scaffold for the complex at the plasma membrane. In that study, the KIF13B FLKO mice showed a modest increase of serum cholesterol and factor VIII, likely due to the reduced uptake of LRP1 bound ligands (24). Based on previous findings demonstrating direct binding of FHA domain of KIF13B to the GAP domain of centaurin-α_1 (8), Kanai

and colleagues proposed a model rationalizing the enhancement of LRP1 endocytosis and its ligands (Figure 1.2). Nonetheless, these studies did not explain how LRP1 binds to hDLG1, and if the CAP-Gly domain of KIF13B plays any functional role in the endocytosis of specific LRP1 ligands.

To that end, we employed two mouse models that were developed by the Chishti lab to evaluate the role(s) the KIF13 family members play in the regulation of LRP1 endocytosis. One mouse model expresses a truncated form of KIF13B lacking only its CAP-Gly domain (KIF13ΔCG), and the other is a full-length KIF13A null (KIF13A FLKO) (Figure 3.1) (unpublished). These models are important tools that allowed us to interrogate the role of the CAP-Gly domain of KIF13B, which was not addressed by the Kanai study, and assess any compensatory role of KIF13A.

1.2 hDLG1 background

In addition to characterizing mice lacking the CAP-Gly domain of KIF13B, we sought to explore the biochemical basis of the LRP1-hDLG1 interaction due to its importance in the linkage to KIF13B and the regulation of LRP1-mediated endocytosis (24).

DLG was originally identified in *Drosophila* as an important developmental gene with tumor suppressor properties; mutations in this gene leads to overgrowth of the imaginal discs cells and contributing to embryonic lethality (28). Other functions of hDLG1 have been linked to cytokinesis, synaptic function, epithelial polarity, and oncogenic or tumor suppressor properties, depending on the subcellular localization of the protein (reviewed in (29)). Mice homozygous for knock-out alleles exhibit neonatal lethality, kidney defects, reproductive organ morphology, and cleft palate (30, 31).

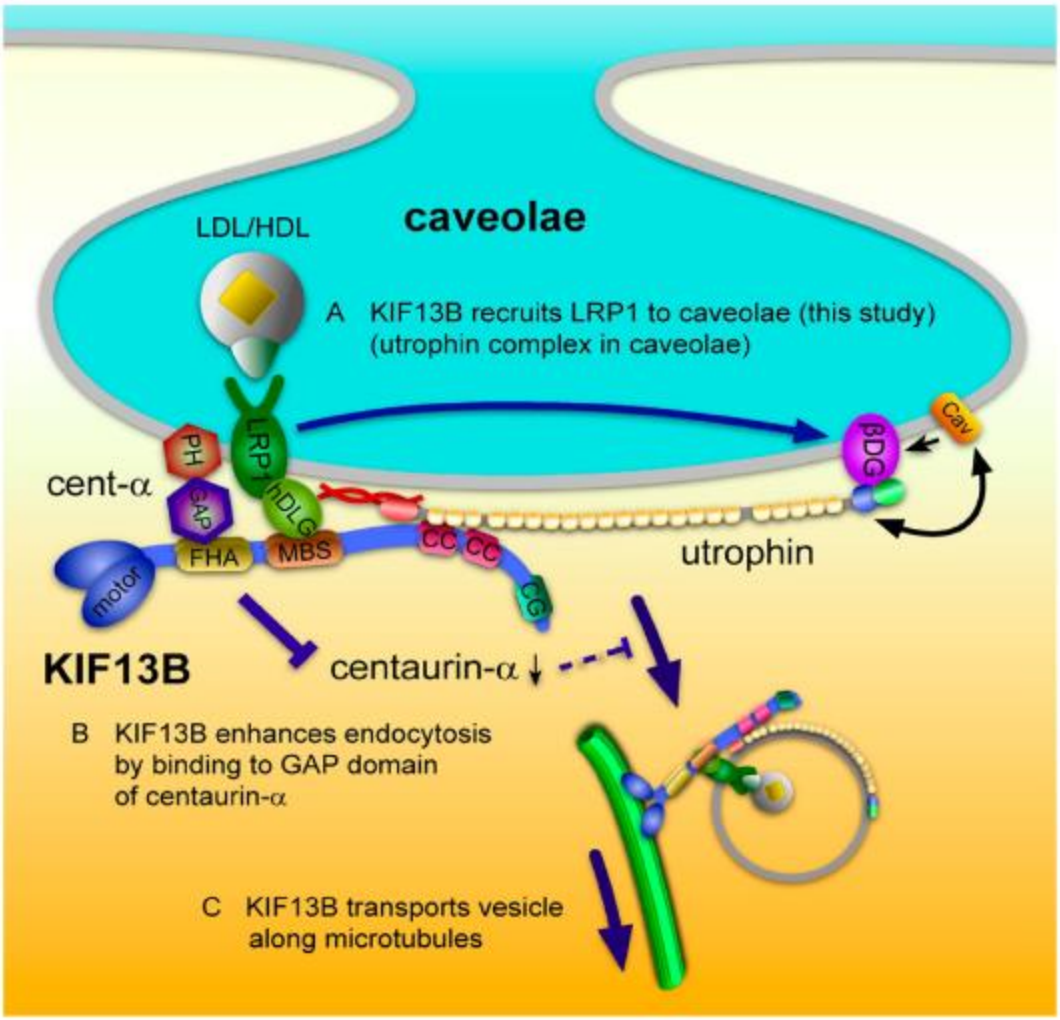

Figure 1.2. Proposed model for the role of KIF13B in caveolin-dependent endocytosis of LRP1. (A) KIF13B links LRP1 to caveolae through the LRP1–hDLG1–KIF13B–utrophin–caveolae linkage. Utrophin complex interacts with caveolin-1 in caveolae and utrophin competes with caveolin for the binding to βDG. (B) KIF13B activates Arf6 through the inhibition of Arf6-GAP activity of centaurin-α1, subsequently enhancing endocytosis nearby. (C) KIF13B, as a motor protein, transports the endocytosed vesicles along microtubules. Reprinted with permission from Kanai Y, Wang D, Hirokawa N. KIF13B enhances the endocytosis of LRP1 by recruiting LRP1 to caveolae. The Journal of cell biology. 2014;204(3):395-408. doi: 10.1083/jcb.201309066.

hDLG1 belongs to the family of MAGUK scaffolding proteins that recruits various signaling proteins to the plasma membrane and is ubiquitously expressed in the mammalian body. Other MAGUK family members include PSD-95 and the MPP subfamily, and are all defined by the presence of one or more PDZ domains, an SH3 domain, and a GUK domain (32). The GUK domain is structurally very similar to guanylate kinases; however, the P-loop that binds ATP is absent, thus rendering it catalytically inactive (28, 33). Instead, this domain adopts a role similar to the PDZ and SH3 domains, and is often involved in protein-protein interactions, such as that of hDLG1's interaction with KIF13B. The SH3 and GUK domains are known to associate with each other by bending as if on a hinge that exists between these domains, leading to a folded conformation. Moreover, hDLG1 contains an N-terminal L27 domain that plays a role in autoregulation, in which the L27 domain folds back and interacts with the SH3-GUK domains, allowing the protein to exist in a compact U-shaped, inactive conformation. This offers the opportunity to regulate its interactions with its binding partners (34).

hDLG1 also contains the alternatively spliced variants insert 2 (I_2) or insert 3 (I_3) located between its SH3 and GUK domains (35). Unlike the I_2 insert, the I_3 insert, encoded by 34 amino acids, contains the sole binding site for the FERM domain of protein 4.1 (36), and is required for the membrane targeting of hDLG1 (36). Importantly, a region termed the HOOK domain located between the SH3 and GUK domains, which is similar to the I_3 sequence in hDLG1, is essential for the membrane localization as well as polarity and overgrowth regulation in *Drosophila* Dlg (33). Additionally, the expression levels of each variant, as well as the subcellular localization of each, correlate with the differentiation state of keratinocytes (37). The hDLG1 I_3 variants are selectively up-regulated during

epithelial differentiation, with a decrease in cytoplasmic I_3 variants, as they are relocated to the cell periphery. This process is accompanied with only a small concomitant reduction of I_2; however, I_2 variants exit the nucleus during differentiation, suggesting that nuclear hDLG1 functions in growth, but not maturation, of keratinocytes (37).

1.3 LRP1 background

KIF13B and hDLG1 interact to form a complex at the cytoplasmic tail of LRP1 (24), but the domains or motifs essential for this interaction are not fully elucidated. We sought to identify the domains of hDLG1 and motifs of LRP1 necessary for this theoretical interaction.

LRP1 is a member of the LDL receptor (LDLr) family that is composed of 2 subunits. The encoded preproprotein is proteolytically cleaved by furin to generate the large extracellular α subunit at 515 kDa and the smaller transmembrane β subunit of 85 kDa that form the mature receptor (38) (Figure 3.8A). LRP1 is ubiquitously expressed in most tissues, with high expression in liver, brain, and fat. Deletion of the LRP1 gene leads to lethality in mice, revealing a critical, but undefined, role in development. Furthermore, expression of this gene decreases with age, and thus many believe LRP1 plays a protective role by clearing excess plasma proteins and maintaining proteostasis (39). Tissue-specific gene deletion studies reveal an important contribution of LRP1 in the vasculature, central nervous system, in macrophages, and in adipocytes, with various roles in vascular permeability and maintenance of the blood-brain barrier, proliferation, cell migration, and lipid homeostasis (reviewed in (39, 40)).

LRP1 is more complex as compared to LDLr; its multiple ligand binding repeats located within the α subunit enable it to recognize nearly 40 different ligands (reviewed in

(39). By far the largest group of ligands that are recognized by LRP1 are either proteinases or molecules associated with regulating proteolytic activity; therefore, LRP1 plays a major role as an endocytic scavenger by mediating extracellular levels of a wide variety of these proteins. For instance, LRP-1-mediated internalization of MMP-2 and MPP-9 is pivotal for controlling the extracellular activity of these major proteinases (41). Additionally, LRP1 plays a critical role in brain amyloid β uptake and degradation, thus suggesting a protective role during the progression of Alzheimer's disease (42). Furthermore, the role of LRP1 in lipoprotein metabolism has been strengthened by independent findings that revealed that LRP1 binds not only to apolipoprotein E-containing particles, such as chylomicron remnants (43), but also the lipases that are directly involved in the generation of the remnant lipoproteins from triglyceride-rich chylomicrons (44). Finally, LRP1 is responsible for mediating catabolism of factor VIII (45), which is important because elevated circulating levels of factor VIII, or its inactivating binding partner von Willebrand factor, predispose the organism to thrombotic complications like venous thrombosis and stroke (reviewed in (46)).

Furthermore, LRP1 regulates multiple signaling pathways in part due to the cytoplasmic tail of its β subunit interacting with a number of adaptor proteins (39). Besides the YxxL motif at tyrosine 4507, which signals for rapid endocytosis through coated pits (47), various proteins bind directly to the cytoplasmic tail of LRP1, giving LRP1 a regulatory role in many signaling pathways, such as the PDGF or TGFβ signaling pathway (40, 48). Specifically, LRP1 controls expression, activity, and trafficking of the PDGF receptor-β in vascular smooth muscle cells and is a receptor for TGFβ1 that is required for TGFβ mediated inhibition of cell proliferation (49). LRP1 can also function as a co-

receptor partnering with other cell surface or integral membrane proteins, for example, the cytoplasmic tail indirectly binds to β-amyloid precursor protein (APP) via the FE65 adaptor (50). LRP1 is necessary for the alpha 2-macroglobulin-mediated clearance of secreted amyloid precursor protein and beta-amyloid, the main component of amyloid plaques found in Alzheimer's patients, and has been found to be lower than controls in brain tissue from Alzheimer's disease patients.

Finally, post-translational modifications of LRP1-cytoplasmic tail have been shown to regulate various interactions with adaptor proteins, particularly via phosphorylation of the tyrosine residues embedded within the two NPxY motifs of LRP1-CT (51-53). Phosphorylation of tyrosine residues at Y4507 and Y4473 located within the two NPxY motifs of LRP1-cytoplasmic tail have been shown to regulate various interactions of LRP1 with adaptor proteins, such as FE65 or SNX17 (51-53). Importantly, the phosphorylation of Y4507 precedes and exposes Y4473 for subsequent phosphorylation reaction (51). Other post-translational modifications to the cytoplasmic tail of LRP1 include the phosphorylation of serine and threonine residues. An example of this regulation is when the serine/threonine residues are not phosphorylated, LRP1 is internalized more rapidly than phosphorylated LRP1, revealing that phosphorylation reduces the association of LRP1 with adaptor proteins of the endocytic machinery (54). In contrast, serine and threonine phosphorylation was necessary for the interaction of LRP with Shc, an adaptor protein that participates in signaling events (54). Furthermore, serine and threonine phosphorylation increased the interaction of LRP1 with other adaptor proteins such as Dab-1 and CED-6/GULP. These results indicate that phosphorylation of LRP1 by PKCα modulates the endocytic and signaling function of LRP1 by modifying its

association with adaptor proteins. (54). Finally, glycosylation of the whole LRP1 protein plays an important role in signaling, and is differentially glycosylated in a tissue-specific manner (55). In particular, carbohydrate addition reduces proteolytic cleavage of the extracellular domain and, concomitantly, the release of the cytoplasmic tail. The extracellular cleavage step that results in the shedding of the LRP1 α is enhanced when the protein is hypo-glycosylated, which in turn results in increased substrate availability for the final γ-secretase-mediated release of the cytoplasmic tail (55).

In this study, we show that the KIF13BΔCG mouse model manifests a relatively higher serum cholesterol phenotype, similar to the KIF13B FLKO mouse (24). In contrast, the KIF13A FLKO mouse model does not show any discernible defect in LRP1 endocytosis. This finding suggests that the CAP-Gly domain of KIF13B is involved in the uptake of lipoproteins, possibly through an LRP1-mediated mechanism. Furthermore, we show that the cytoplasmic tail of LRP1 interacts specifically with the alternatively spliced I_3 sequence of hDLG1, and this interaction was not affected by the disruption of tyrosine phosphorylation of LRP1 at tyrosine 4507. These results reveal a novel function of the CAP-Gly domain of KIF13B in receptor-mediated endocytosis and begin to clarify the biochemical basis of LRP1-hDLG1 interaction required for recruitment of the membrane macromolecular complex.

Chapter 2: MATERIALS AND METHODS

2.1. Materials

DMEM (11995-065) and FBS (10437-028) were obtained from Gibco. LPDS was made as previously described (56). FuGENE 6 used for transfections was from Promega (E2693). LRP1-Herz was obtained from Dr. Joachim Herz, University of Texas Southwestern Medical Center (57). [^{3}H]Cholesteryl oleate (NET746) and [^{3}H] oleate (NET289) were obtained from Perkin-Elmer. Mouse IgG was from Santa Cruz (sc-2025), Hoechst stain was from Calbiochem (382061), and the following antibodies were obtained as follows: LRP1 from Abcam (ab92544), β-Actin from Sigma (A5316), hDLG1 mAb 2D11 was previously developed as described (58), rabbit KIF13B N-terminus 1246 was previously developed as described (7), Streptavidin-HRP from Pierce (21124), Na^+/K^+ ATPase from Abcam (ab2873), mouse mAb anti-β-Tubulin antibody from Sigma (T4026), secondary antibodies: Goat Anti-Rabbit HRP conjugate (170-5046) and Goat Anti-Mouse IgG HRP conjugate (170-6516) from Bio-Rad, Alexa Goat Anti-Rabbit 568 from Invitrogen (948491), and Biotin-SP AffiniPure Donkey Anti-Rabbit IgG (711-065-152) and Cy3 Streptavidin (016-160-084) from Jackson ImmunoResearch Labs. Normal donkey block (NDB: in PBS, 10% Normal Donkey Serum,5% Non-Fat Dry Milk, 4% BSA, 0.1% TritonX-100) was a gift from the Schwob lab at Tufts University School of Medicine. ECL Prime Western Blotting Detection Reagent was from GE Healthcare (RPN2232). Chromogenix Coatest SP4 Factor VIII assay was from Diapharma (82409463). Phusion PCR kit was from NEB (M0530S). Glutathione Sepharose beads were from GE Healthcare (17-0756-01). Primers were designed in house and ordered through Tufts University Core Facility. MEFs were isolated from mice as described below. HEK293T and HepG2 cells

originally obtained from American Type Culture Collection. Restriction enzymes and buffers were from New England Biolabs. EconoTaq used for genotyping was purchased from Lucigen (F93366).

2.2. Mouse studies

2.2.1. Generation of mouse models

ES cell clones with targeted alleles for KIF13A (AF0553) and KIF13B (AF0005) were obtained from the Knockout Mouse Project Repository at the University of California, Davis. Mouse lines were created in Tufts University Transgenic Animal Core Facility. We are grateful to Dr. Janis Lem, Director of the Transgenic Core Facility, for generously providing technical advice and training during the embryonic stem cell culture, electroporation, and colony selection protocols. Primers used for genotyping are:

13aF1 (5'-CATGTGGCCCTTGAACTTGCAAAG-3'),

13aR1 (5'-CTTTAGCTCGGGGGCCTTCATGGC-3'),

13aF2 (5'-AGGGAGCAGCTCTCGCAGGCTGAG-3'),

13aGeoR (5'-CCCTGGATATGGCAGTCTCTAC-3'),

13bF1 (5'-AAAGCCTAATGCAAGGCTGGGAG-3'),

13bR1 (5'-AGAGTGAAGGCAGACTAAAGATGG-3'),

13bGeoR (5'-ATGAGGGAGCAGGGCTCG-3').

2.2.2. Measurement of serum lipids in mice

Serum was harvested from WT (n=10), KIF13BΔCG (n=11), and KIF13A FLKO (n=6) male mice of average age 4 months via terminal bleed from the vena cava. The blood was allowed to clot for 30 minutes and serum was collected after centrifugation. The serum

was analyzed for total cholesterol, LDL, and HDL. Serum triglycerides and VLDL were determined in the subset of wild-type (n=5) and KIF13BΔCG (n=6) male mice that were fasted for eight hours before serum collection. These experiments were performed by the Jean Mayer USDA Human Nutrition Research Center on Aging core facility at Tufts University.

2.2.3. Measurement of plasma factor VIII in mice

To measure factor VIII in plasma, blood was harvested from 6-month old wild-type (n=5) and KIF13BΔCG (n=6) male mice via terminal bleed from the vena cava in the presence of acid citrate dextrose (1:10 dilution) as an anticoagulant. Plasma was collected within 30 minutes of harvest by centrifugation and used in the factor VIII assays. The timed clot formation assay was performed similar to the activated partial thromboplastin time (aPTT) assay from (59) and (60). Briefly, mouse plasma was mixed in a two-step method with clot activating components and a fibrometer was used to measure the time until a clot was formed. Mouse plasma samples were added to plasma mix (20% phosphatidylserine phospholipid vesicles) and incubated for five minutes at 37°C. Activation mix ($CaCl_2$ and factor XIa as an activator in Tyrode's Buffer) was added and the timer was immediately started. The longer the time for a clot to form indicates less factor VIII activity. These experiments were performed at the Boston VA Hospital in the Gilbert lab by Madhumouli Chatterjee. The chromogenic assay was performed on the same samples in parallel using the Chromogenix Coatest SP4 Factor VIII kit (Diapharma) per manufacturers' instructions.

2.2.4. Liver histology and immunohistochemistry

Liver tissue from 6-month old wild-type and KIF13BΔCG mice were harvested and stored either flash frozen in OCT compound or fixed in 10% formalin for three days. Paraffin embedding, sectioning, and Hematoxylin & Eosin staining were performed at the Tufts Medical Center Pathology Core Facility and pathological analysis of the Hematoxylin & Eosin slides was performed by Roderick Bronson at Harvard Medical School. Paraffin-embedded brain and liver sections were deparaffinized and rehydrated, and antigen retrieval was accomplished using sodium citrate. Autofluorescence was quenched using quenching solution (2.5 mg/ml ammonium chloride in TBS). Tissues were blocked using Normal Donkey Block and were incubated with a rabbit polyclonal antibody against the N-terminus of KIF13B at a dilution of 1:200 (7) overnight at 4°C. Tissues were then incubated for one hour each in biotinylated donkey anti-rabbit secondary antibody and then Streptavidin anti-donkey Cy3 tertiary antibody. Tissues were washed thoroughly with PBS after each incubation, and nucleus was counterstained with Hoechst and mounted with 90% glycerol in PBS. Slides were visualized and photographed at 40X using Zeiss Axio Imager.M2 microscope and AxioCam MRm and MrC using AxioVision version 4.8 software. The exposure time and sharpness were kept consistent across all photos. Control slides with secondary and tertiary antibodies only were used to assess the background staining.

2.2.5. Fibroblasts establishment

MEFs were prepared from day 13.5 embryos and maintained in DMEM with 10% FBS. KIF13BΔCG and KIF13A FLKO mice were backcrossed to almost pure C57BL/6J

background. MEFs from KIF13A FLKO crossed with KIF13BΔCG (DKO) were prepared from mixed C57BL/6 x 129 genetic background mice.

2.3. Cell culture

2.3.1. LRP1 immunofluorescence

MEFs were seeded on coverslips in DMEM containing 10% FBS for 3 days and fixed with 3% paraformaldehyde/PBS. Cells were permeabilized with 0.3% TritonX-100 and blocked with Normal Donkey Block for one hour. Cells were incubated overnight at 4^{o}C in Rabbit anti-LRP1 mAb from Abcam diluted 1:5000 in Normal Donkey Block. Cells were then incubated for one hour each in biotinylated donkey anti-rabbit secondary antibody and then Streptavidin anti-donkey Cy3 tertiary antibody. Cells were washed thoroughly with PBS after each incubation, and nucleus was counterstained with Hoechst and mounted with 90% glycerol in PBS. Cells were visualized and photographed at 40X using Zeiss Axio Imager.M2 microscope and AxioCam MRm and MrC using AxioVision version 4.8 software. The exposure time and sharpness were kept consistent across all photos. Control cells with secondary and tertiary antibodies only were used to assess the background staining.

2.3.2. LRP1 Western blotting

Cleared lysates from human umbilical vein endothelial cells and wild-type, KIF13A FLKO, KIF13BΔCG, and KIF13 DKO MEFs were analyzed for steady state LRP1 protein expression by Western blotting. Lysates from above mentioned cells were harvested with NP40 containing lysis buffer with multiple phosphatase and protease inhibitors on ice before sonication and centrifugation to remove cell debris. The BCA

method was used to determine total protein concentration. Protein (25 µg) was loaded onto a 4-12% Bis Tris gel and transferred to a nitrocellulose membrane. After briefly staining with Ponceau S to confirm acceptable transfer of proteins and rinsing with TBS-Tween, the membrane was blocked with 5% milk for one hour and incubated with rabbit mAb LRP1 at a dilution of 1:50,000 from Abcam in 5% milk overnight at 4°C. After multiple rinses with TBS-Tween, the secondary antibody HRP-conjugated goat anti-rabbit from Bio-Rad in 5% milk was applied for one hour at room temperature. After multiple washes with TBS-Tween, ECL luminating solution was applied to the membrane and then exposed to film and developed.

2.3.3. LPDS, LDL, [^{3}H]-LDL, and [^{3}H]-Cholesteryl oleate production

Lipoprotein deficient serum (LPDS) was prepared by ultracentrifugation of FBS to remove LDL from the serum as previously described, omitting the thrombin incubation (56) before being used in the growth media. LDL was isolated from human blood by ultracentrifugation as previously described (56). [^{3}H-CO] LDL was made by combining [^{3}H] cholesteryl oleate and isolated human LDL as previously described (61) at a specific activity around 30 dpm/pmol. [^{3}H] oleate was prepared by combining with fatty acid free bovine serum albumin as previously described (56) with a specific activity around 21 dpm/pmol.

2.3.4. [^{3}H]-LDL uptake and hydrolysis assay

MEFs were seeded in DMEM containing 10% LPDS and cultured for 3 days. Cells were then incubated with 50 µg/ml [^{3}H]CO-LDL for 3, 4.5, 6, and 7.5 hours. Lipids were extracted with hexane:isopropanol (3:2) solvent and dried under air. Each sample was

resuspended in chloroform:methanol (2:1) and thin layer chromatography was performed on silica plates in toluene:ethyl acetate (2:1). [^{3}H]-labeled cholesterol and cholesteryl esters were quantified and normalized relative to the amount of protein per well. The uptake was determined as the sum of labeled cholesterol and cholesteryl esters, and the hydrolysis of LDL was determined as the fraction of labeled cholesterol over total labeled uptake. Each experiment was run in triplicate.

2.3.5. Cholesterol esterification assay

MEFs were seeded in DMEM + 10% LPDS and cultured for 4 days. The cells were then incubated with varying concentrations of LDL for 8 hours. MEFs were then pulsed with [^{3}H] oleate for 2 hours. Lipids were extracted with hexane:isopropanol (3:2) and dried under air. Each sample was resuspended in chloroform:methanol (2:1) and thin layer chromatography was performed on silica plates in heptane:diethyl ether:glacial acetic acid (90:30:1). [^{3}H] Oleate incorporation into cholesteryl [^{3}H] esters and [^{3}H] triolein was quantified and normalized to the amount of protein. Each experiment was run in duplicate.

2.3.6. Surface protein biotinylation

This protocol was adapted from bio-protocol and Huang *et al* (62). MEFs were plated on poly-dL-Ornithine-coated plates on Day 0. On day 2, at approximately 95% confluency, the monolayer was rinsed with PBS +$CaCl_2$ and $MgCl_2$. Cells were incubated on a rocker at 4°C with 0.5 Sulfo-NHS-SS-biotin solution for 30 minutes before quenching unbound biotin with 50 mM glycine in PBS+$CaCl_2$ and $MgCl_2$. Cells were scraped and collected in lysis/IP buffer (in PBS: 5 mM EDTA, 5 mM EGTA, 10 mM sodium Pyrophosphate, 50 mM NaF, 1 mM $NaVO_3$, 1% Triton, 1 tablet protease inhibitor) and set

on ice for 30 minutes. Cleared lysates were used to load 600 µg of protein onto NeutrAvidin beads in IP buffer and left rotating at 4°C overnight. Beads were washed by rotation three times for five minutes in IP buffer and boiled at 65°C for 10 minutes before loading for Western blotting. Protein was transferred from 4-12% Bis-tris gel onto a nitrocellulose membrane. The membrane was blocked in 5% milk in TBS-Tween and blotted with various antibodies: Streptavidin-HRP to confirm biotinylation of total (and only) surface proteins, anti-LRP1, anti-β actin for cytoplasmic control, and anti-Na^+/K^+ ATPase for the membrane loading control.

2.4. Cloning and protein interaction assays

2.4.1. Cloning and site directed mutagenesis

LRP1-Herz plasmid was a gift from Dr. Joachim Herz at the University of Texas Southwestern Medical Center (57). This plasmid includes a portion of LRP1-β from 13201 bp to 14247 bp in a pcDNA3.1/Zeo backbone, which translates a protein that includes six extracellular EGF-like domains (223 extracellular amino acids), the transmembrane domain, and the cytoplasmic tail (Figure 3.8A). To generate LRP1- Herz and LRP1-CT constructs tagged with Thioredoxin (TRX), primers for LRP1-Herz or LRP1-CT containing BamHI or EcoRV restriction sites (Figure 3.8A) were used in Phusion High Fidelity PCR using LPR1-Herz plasmid as the template. LRP1-CT forward (5'- GCG-GGATCC-AAG CGG CGA GTC CAA GGG GCT-3'), LRP1-Herz forward (5'-GCG-GGATCC-CGG CCT GGA ACC TGT AAC CTG-3'), and LRP1 reverse (5'-GCG-GAATCC-CTA TGC CAA GGG GTC CCC TAT-3'). The pET32a plasmid with the TRX tag and PCR products were digested with enzymes EcoRV and BamHI and ligation

products were used to transform *E. coli* DH5α. PCR with the pET32a forward and LRP1 reverse primers was used to confirm the inclusion of correct in the pET32a backbone. Successfully transformed colonies were expanded for mini preps to transform *E. coli* BL21 (DE3). TRX-tagged protein expression was induced for three hours with 200 µM IPTG in BL21 cells. TRX and TRX-LRP1-CT were purified on a Nickel column using HPLC and pure fractions were confirmed by SDS-PAGE on 4-12% Bis-tris gel and Coomassie staining. Expression of TRX and TRX-LRP1-CT was analyzed by SDS-PAGE: Coomassie staining of the gel, and Western blotting with anti-TRX antibody with Ponceau S staining of the membrane.

Mutagenesis to convert tyrosine-4507 in the CT tail of LRP1 to phenylalanine (phospho-dead mutation) was performed using Quik Change II Site Mutagenesis Kit with Phusion High Fidelity PCR with primers containing the targeted mutation (mutated nucleotide in bold italics forward: 5'-ccaacttcaccaaccccgtgt***t***tgccacactct-3', reverse: 5'-agagtgtggca***a***acacggggttggtgaagttgg-3'). The LPR1-Herz plasmid was used as the template. All plasmids were sequenced by the Tufts University Core Facility.

2.4.2. Pull-down assays

Previously designed GST-tagged hDLG1 constructs (4, 9, 10) were used for pull-down assays. The GST-fusion proteins were expressed in *E. coli* BL21(DE3) and purified using Glutathione-Sepharose beads (GE). The hDLG1 fusion proteins were immobilized on the beads as bait and incubated with either purified TRX or purified TRX-LRP1-CT protein, or lysates from HEK293T cells transfected with either LRP1-Herz or LRP1-Y4507F with Promega FuGENE 6 transfection reagent as prey. Cleared lysates from transfected HEK293T cells were harvested with NP40 detergent containing lysis buffer

with multiple phosphatase and protease inhibitors on ice before centrifugation to remove cell debris. The BCA method was used to determine total protein concentration. Protein was eluted from the beads by boiling at 90°C for 10 minutes and analyzed by SDS-PAGE on 4-12% Bis-Tris gel. Upon protein transfer, the nitrocellulose membrane was incubated briefly with Ponceau S to determine appropriate transfer and GST construct expression before being rinsed with TBS-Tween and immunoblotted with rabbit anti-LRP1 monoclonal antibody from Abcam as described above in LPR1 Western Blotting.

2.4.3. Co-Immunoprecipitation

HepG2 cells, an immortalized cell line from human liver carcinoma, were homogenized in the subcellular fractionation buffer (20 mM Tris-HCl, pH 7.4, 10 mM KCl, 2.0 mM $MgCl_2$, 1.0 mM EDTA and protease inhibitors), and nuclei pellet was removed by centrifugation at 720 x g for 5 minutes. The membrane fraction was collected by further centrifugation at 100,000 x g for one hour and dissolved in the lysis buffer (20 mM Tris-HCl, pH 7.4, 150 mM NaCl, 0.2% Triton X-100, protease inhibitors). Antibodies used for immunoprecipitation (IP) included anti-hDLG1 mAb 2D11 (58), anti-KIF13B mAb 4A5 (7), and normal mouse IgG (Santa Cruz). Protein A/G PLUS-Agarose (Santa Cruz) beads were used to recover the immune-complex, analyzed by SDS-PAGE and Western blotting with an anti-LRP1 rabbit mAb (Abcam).

2.5. Statistical analysis

Data are presented as the mean ± standard deviation. Statistical comparisons were made using analysis of variance (ANOVA) and paired student's t-tests in R and Prism. A P value < 0.05 was considered statistically significant.

Chapter 3: RESULTS

3.1. Mouse Characterization

3.1.1. Generation of KIF13A and KIF13B mouse models

Two mouse models were developed by the Chishti lab to evaluate the role(s) the KIF13 family members play in various systems. One mouse model expresses a truncated form of KIF13B lacking only its CAP-Gly domain (KIF13ΔCG), and the other is a full-length KIF13A null (KIF13A FLKO) (Figure 3.1) (unpublished). These models are important tools that allowed us to interrogate the role of the CAP-Gly domain of KIF13B, which was not addressed by the Kanai study (24), and assess any compensatory role of KIF13A.

KIF13A FLKO and KIF13BΔCG mice were generated by inserting a β-Geo cassette within each of the respective genes. The genotype and protein expression were verified through PCR and Western blotting (Figure 3.1 A & B insets). The insertion of the β-Geo cassette in the KIF13A gene leads to complete knockout of the gene (Figure 3.1A, top right inset), leading to no protein expression (Figure 3.1A, bottom right inset). The insertion of the β-Geo cassette in the KIF13B genomic locus leads to a truncation of the gene, and expression of the truncated protein missing the CAP-Gly domain (Figure 3.1B). The mutant KIF13B protein was not detectable by Western blotting (Figure 3.1B bottom right insert) due to the β-Geo insert increasing the size of the protein beyond what can be transferred and/or the epitope recognized by the monoclonal antibody was removed with the deletion. To that end, the expression of truncated KIF13B protein was verified by the LacZ staining of embryos and mouse embryonic fibroblasts (MEFs) (Figure 3.1 C & E). In confluent culture of fibroblasts isolated from mutant KIF13BΔCG day 13.5 embryos,

the KIF13B-LacZ fusion protein was observed as intracellular blue dots near the nucleus resembling the microtubule-organizing center. Counterstaining with anti-β-Tubulin antibody showed that the blue dots coincide with the center of microtubule arrays (Figure 3.1E top, arrowheads). Interestingly, in the scratch induced migrating fibroblasts, the blue stain diffused throughout the cells, with significant accumulation at the leading edge (Figure 3.1E bottom, arrowheads). This pattern of KIF13B-LacZ staining is consistent with the reported endogenous localization of hDLG1 and KIF13B at the leading edge of migrating cells (29, 63). This finding suggests the motor function of KIF13BΔCG is still preserved and can move along the microtubules in an anterograde manner.

Both KIF13A FLKO and KIF13BΔCG mice were viable, born at normal Mendelian ratios, and developed to adulthood. To assess the compensatory role of KIF13B and KIF13A, the Chishti lab attempted to generate a double mutant mouse model in C57BL/6J background by crossing of KIF13A FLKO and KIF13BΔCG mice (DKO). Morphological analysis of the embryos at E14.5-E15.5 did not reveal dying/dead embryos. However, high mortality after birth was observed in the DKO mice. Most of the new born pups were either dead or cannibalized, and therefore no viable pups could be recovered after day one. Occasionally, newborn pups were found dead at day one (Figure 3.1D). These pups seem to have their stomachs filled with air without any milk (Figure 3.1D asterisks), suggesting that they are unable to suckle milk properly. Interestingly, morphological evaluation of dead pups revealed relatively short nose appearance and potential craniofacial developmental anomalies that could be the underlying cause of their inability to properly suckle (Figure 3.1D arrowheads). This developmental phenotype appears to be similar to the craniofacial anomalies and cleft palate phenotype observed in mouse Dlg1 mutant

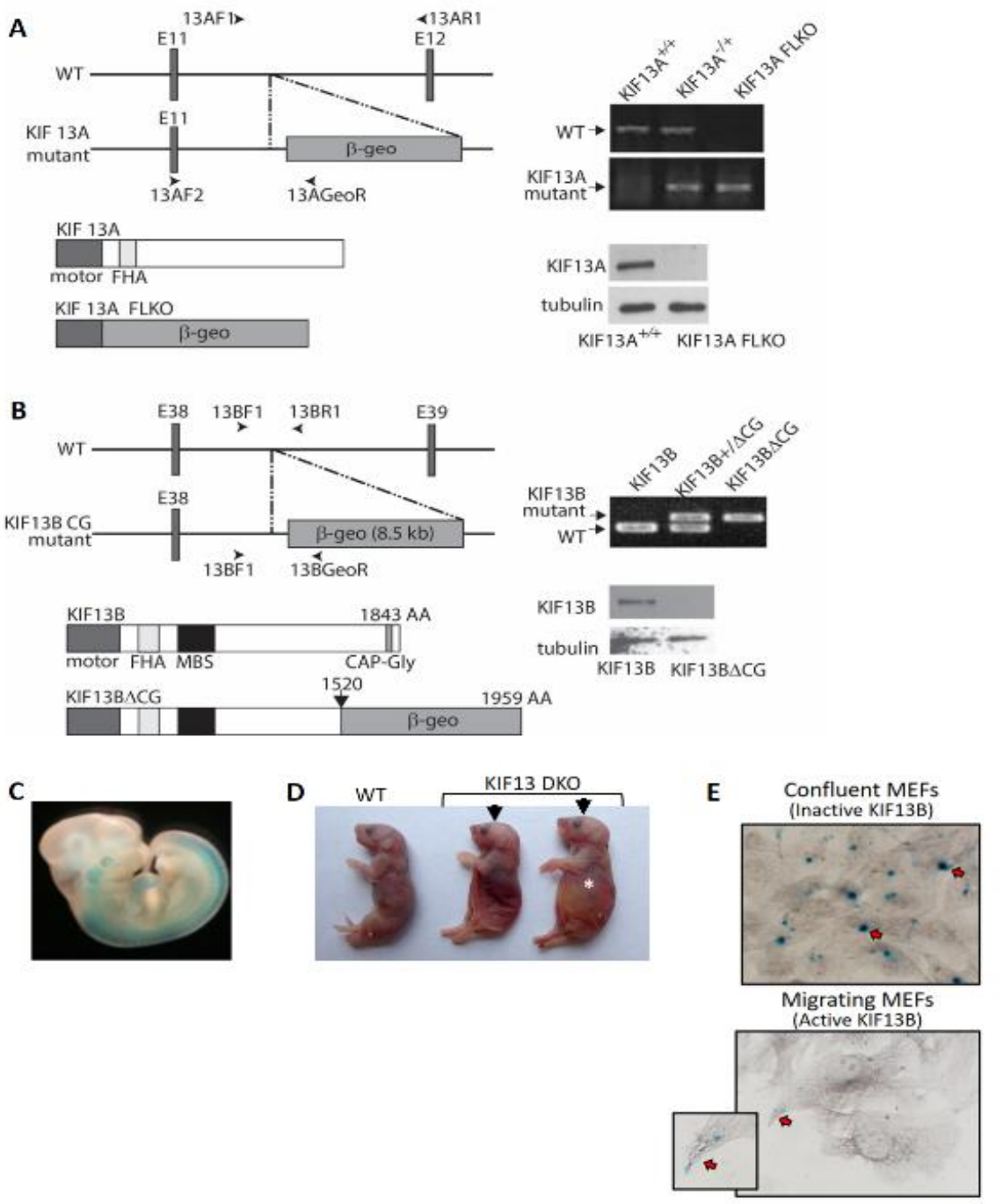

Figure 3.1. Mouse model development and verification. Diagrams of A) KIF13A FLKO and B) KIF13BΔ CG mouse model production by β-geo cassette insertion and verification by PCR (top right of panel) and Western blot (bottom right of panel.) C) LacZ staining showing expression of truncated KIF13B protein in KIF13BΔCG embryo E13.5. D) Representative image of newborn WT and KIF13 DKO pups. Arrowheads indicate face deformity (short snout), and asterisk indicates milk-less stomach full of air. E) LacZ

(Figure 3.1 continued from page 26) staining in MEFs from KIF13BΔCG mice. Top image is a confluent culture, thus KIF13B appears to be inactive. Bottom image is after a scratch assay is initiated to activate cell migration, thus activating KIF13B and changing the subcellular localization. Inset of right image is an enlarged frame of the leading edge of the fibroblast. Orange arrows discern the change of location of KIF13B in confluent versus migrating MEFs.

mice (30, 31). The initial analysis of two dead pups recovered at day one did not show any discernible evidence of cleft palate. However, the lab did not pursue further characterization of the dead newborn DKO mice since the colony of DKO mice was not sustainable.

3.1.2. Effect of CAP-Gly domain deletion in mice on cholesterol and factor VIII phenotype

A previous study has shown that KIF13B FLKO mice exhibit increased levels of serum cholesterol and plasma factor VIII, which are known ligands of LRP1 (24). We measured the levels of serum lipids and plasma factor VIII in our KIF13BΔCG mouse model to determine if the CAP-Gly domain was required for maintaining the homeostasis of these LRP1 ligands. The levels of total serum cholesterol, LDL, HDL, vLDL, and triglycerides (Figure 3.2) were analyzed from wild-type, KIF13BΔCG, and KIF13A FLKO mice. The KIF13BΔCG mice, lacking the CAP-Gly domain, showed significantly elevated levels of total cholesterol ($p = 0.033$), LDL ($p = 0.0051$), and HDL ($p = 0.067$) as compared to wild-type mice, when analyzed using the two-tailed unpaired t test. The F test to compare variances was not significant for total cholesterol and HDL measurements; however, it was significant for the LDL measurements; therefore, the Welch's correction was administered in the two-tailed unpaired t test. In contrast, the levels of VLDL and triglycerides were not

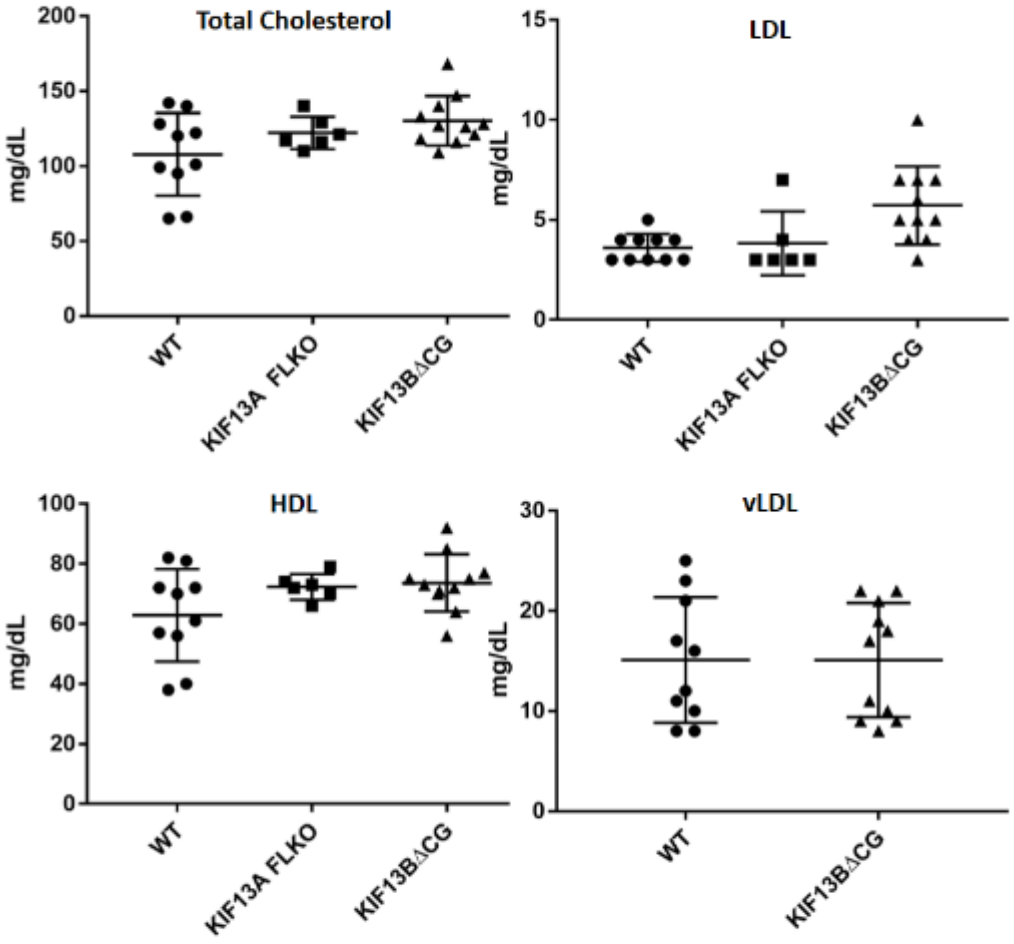

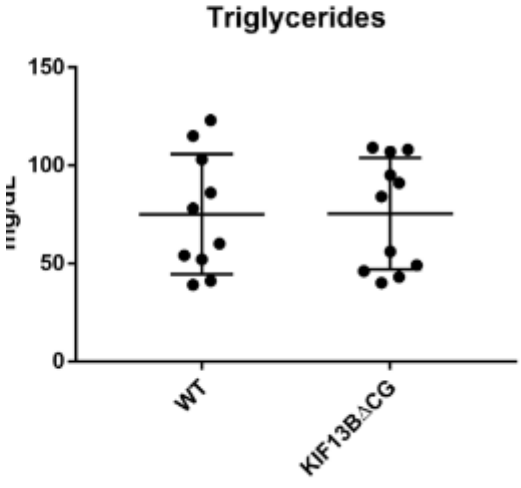

Figure 3.2. Characterization of mouse lipid profile. Total cholesterol, direct measurement of LDL, and HDL of wild-type (WT), KIF13A FLKO, and KIF13BΔCG mouse serum, and vLDL and triglyceride measurement of WT and KIF13BΔCG mouse serum after 6 hour fasting. N= 10 WT, 11 KIF13BΔCG, 6 KIF13A. Significant p values between WT and KIF13BΔCG: Total: p= 0.033, LDL: p= 0.0051, HDL: p=0.067. Error bars represent the SEM.

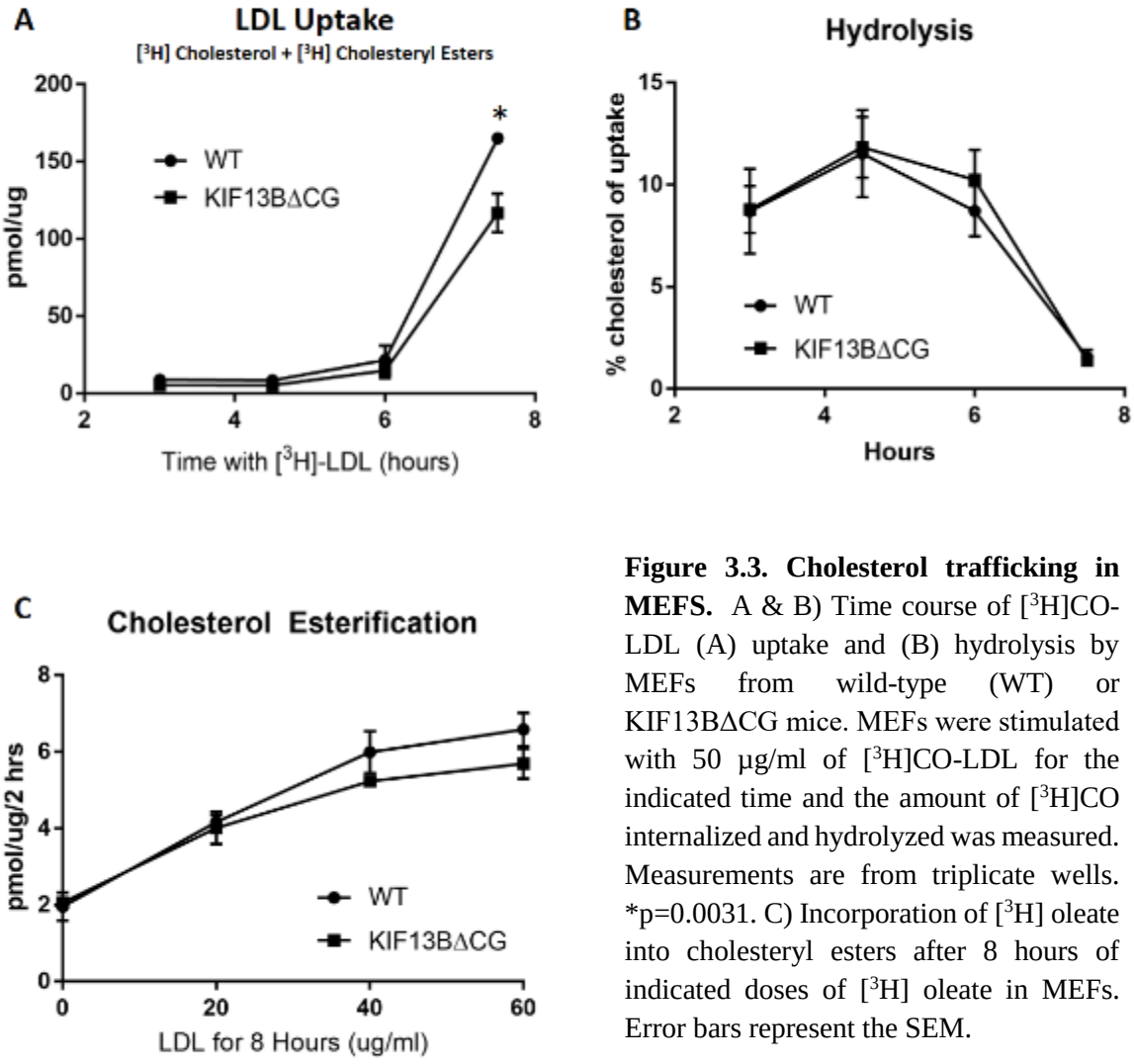

Figure 3.3. Cholesterol trafficking in MEFS. A & B) Time course of [^{3}H]CO-LDL (A) uptake and (B) hydrolysis by MEFs from wild-type (WT) or KIF13BΔCG mice. MEFs were stimulated with 50 µg/ml of [^{3}H]CO-LDL for the indicated time and the amount of [^{3}H]CO internalized and hydrolyzed was measured. Measurements are from triplicate wells. *p=0.0031. C) Incorporation of [^{3}H] oleate into cholesteryl esters after 8 hours of indicated doses of [^{3}H] oleate in MEFs. Error bars represent the SEM.

significantly different between fasted wild-type and KIF13BΔCG mice, nor did the KIF13A FLKO mice show any measurable difference in the levels of these lipids as compared to wild-type mice. To further investigate the biochemical basis of the observed cholesterol phenotype, we measured the uptake of [^{3}H]CO-LDL in MEFs derived from wild-type and KIF13BΔCG embryos. The uptake and hydrolysis of [^{3}H]CO-LDL in MEFs indicate that KIF13BΔCG MEFs exhibit only slightly decreased uptake of [^{3}H]CO-LDL at later time points (Figure 3.3A). Hydrolysis of the LDL-derived [^{3}H]CO appeared normal (Figure 3.3B) as did cholesterol esterification (Figure 3.3C).

In addition, we measured plasma factor VIII levels in wild-type and KIF13BΔCG mice either by the timed clot assay (Figure 3.4A) or Chromogenix colorimetric assay (Figure 3.4B). We did not find any significant difference in the factor VIII levels between wild-type and KIF13BΔCG mice using these assays. It is to be noted that although the difference was not statistically significant, nearly half of the KIF13BΔCG mice showed elevated levels of serum factor VIII activity. The standard deviation for KIF13BΔCG in each assay was much greater than that of the wild-type results (timed clot assay: wild-type average= 411.2±27.33 seconds, KIF13BΔCG average 465.8±44.62 seconds. Chromogenic assay: WT average 98.8±27.1 units/ml, 22.4% activity, SD ±6.2, KIF13BΔCG average 103.6±72 units/ml, 23.5% activity, SD ±16.4.) To resolve whether the CAP-Gly domain of KIF13B plays a functional role in the uptake of factor VIII would require a larger cohort of age and sex matched KIF13BΔCG mice in future studies.

3.1.3. Liver histology

Paraffin-embedded liver sections were stained with hematoxylin and eosin to determine if the CAP-Gly domain deletion of KIF13B leads to morphological changes,

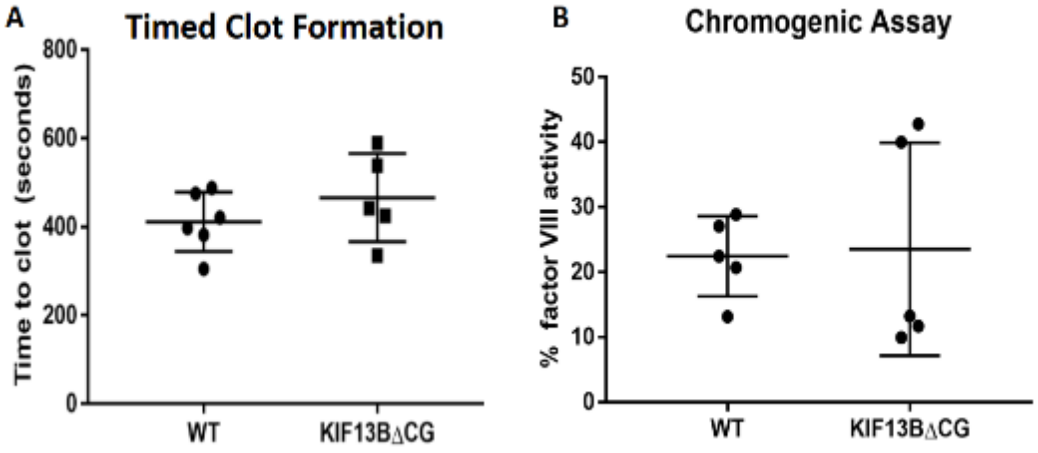

Figure 3.4. Characterization of mouse factor VIII levels. A) Timed clot assay to measure Factor VIII activity in wild-type (WT) and KIF13BΔCG mouse plasma n=5. B) Chromogenic assay of same samples to measure factor VIII activity. 100% is equivalent to 1 IU/ml of factor VIII. Error bars represent the SEM.

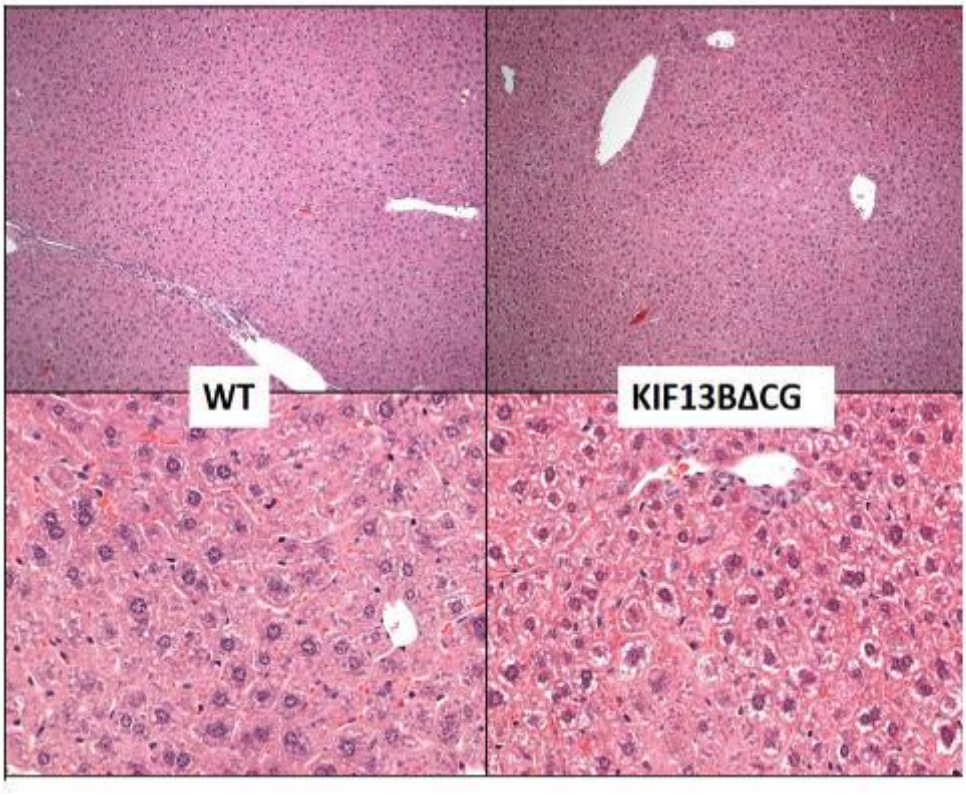

Figure 3.5. Characterization of mouse liver histology. Paraffin-embedded livers from wild-type (WT) and KIF13ΔCG mice were H&E stained. No pathological anomalies were identified. Pictures were taken at 10x (top) and 40x (bottom).

such as fibrosis or fatty deposits as would be seen in an animal with elevated cholesterol levels. No pathogenesis was found in these livers, even in mice over 12 months of age (Figure 3.5). To exaggerate a possible phenotype, both wild-type and KIF13BΔCG mice could be put on a high fat diet to see if the mutant's liver is more affected by the diet in future studies.

3.1.4. Effect of CAP-Gly domain deletion on KIF13B protein localization

The subcellular localization of KIF13B protein in WT and KIF13ΔCG mice was analyzed in the brain tissue sections by immunofluorescence microscopy using a polyclonal antibody that recognizes the N-terminus of KIF13B protein. As shown in figure 3.6A, there is a punctate staining pattern of the protein in both mice; however, the puncta in the KIF13BΔCG mice is less localized in the perinuclear region as compared to wild-type. In addition, the expression of truncated KIF13B protein appears to be substantially reduced compared to the expression level of wild-type KIF13B (Figure 3.6A). This observation suggests that the deletion of the CAP-Gly domain causes the KIF13B protein to be mislocalized. Since KIF13B is abundantly expressed in the liver, we also analyzed localization in liver tissue from wild-type and KIF13BΔCG mice. However, auto-fluorescence of liver tissue prevented from visualizing normal and truncated KIF13B (Figure 3.6B). Of note, a monoclonal antibody previously generated against the C-terminus of KIF13B (7) cannot be used for these experiments since its epitope is missing in the truncated KIF13B protein of KIF13BΔCG mice. In future studies, high resolution live imaging and immune-gold electron microscopy approaches would be required to determine

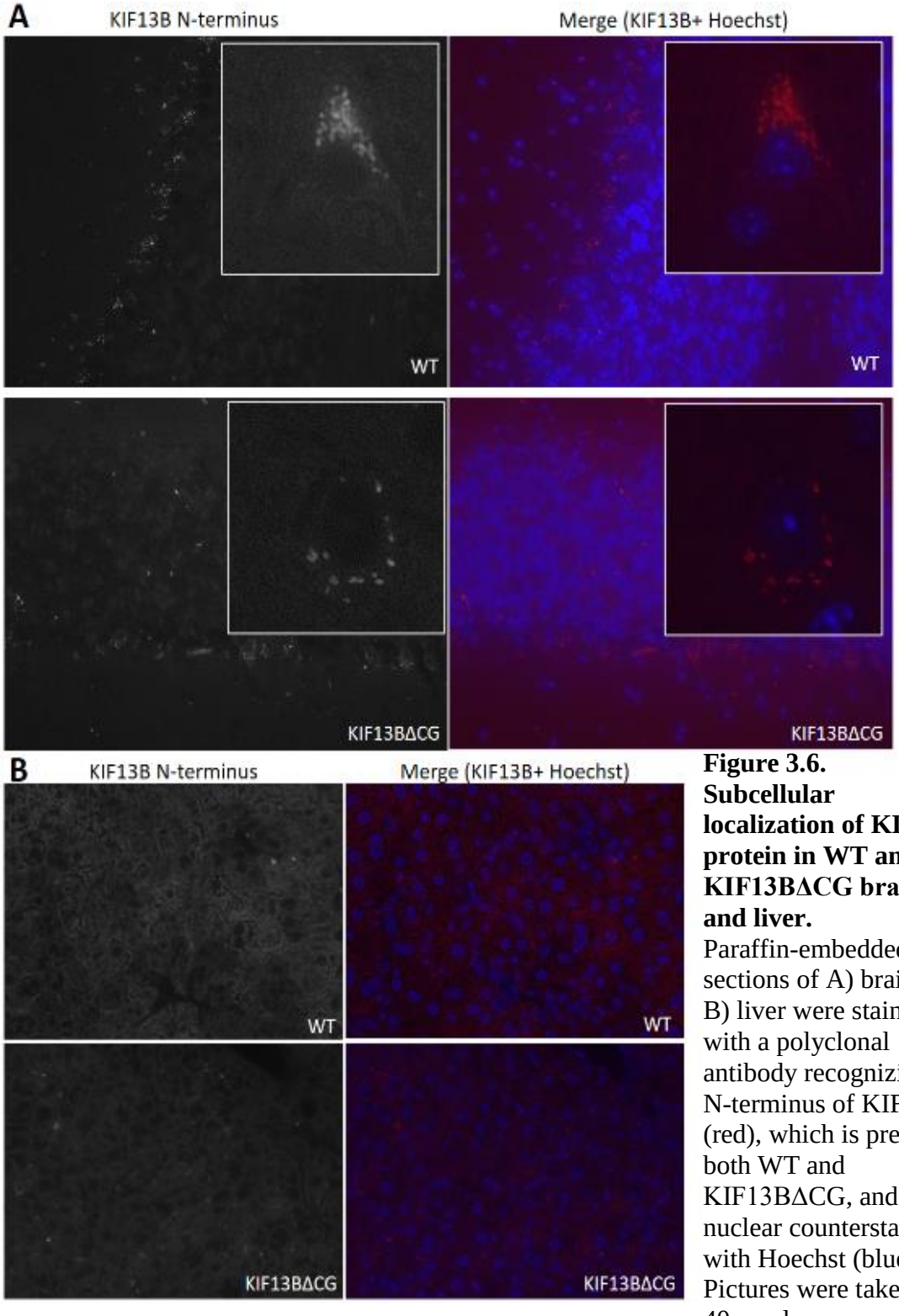

Figure 3.6. Subcellular localization of KIF13B protein in WT and KIF13BΔCG brain and liver. Paraffin-embedded sections of A) brain and B) liver were stained with a polyclonal antibody recognizing the N-terminus of KIF13B (red), which is present in both WT and KIF13BΔCG, and nuclear counterstain with Hoechst (blue). Pictures were taken at 40x and a representative frame was enlarged (insets A).

the precise subcellular compartments of KIF13B protein in wild-type and KIF13BΔCG mice.

3.2 Cell culture studies

3.2.1. LRP1 status in fibroblasts lacking KIF13B CAP-Gly domain

The mislocalization of the KIF13BΔCG protein leads to the hypothesis that the localization of LRP1 may be disrupted as well, due to the suggested interaction of these proteins. MEFs from wild-type, KIF13A FLKO, and KIF13BΔCG mice were used to visualize LRP1 by immunofluorescence microscopy. LRP1 staining appears to be more diffuse in the KIF13BΔCG MEFs as compared to wild-type MEFs in which LRP1 punctate staining is more intense (Figure 3.7A). In contrast, LRP1 staining in the KIF13A FLKO was similar to wild-type. The diffuse staining of LRP1 in KIF13BΔCG MEFs could result from either quantitatively less LRP1 protein in these cells or a redistribution of LRP1 from endosomal vesicles to the cell surface.

If the protein levels of LRP1 were different in wild-type and KIF13BΔCG MEFs, this may reflect decreased stability or decreased synthesis of the LRP1 protein due to the truncated KIF13B protein. Using Western blotting on whole cell lysates from wild-type, KIF13A FLKO, KIF13BΔCG, and KIF13 DKO MEFs, we found the steady state protein expression of LRP1 was not different in MEFs of different genotypes (Figure 3.7B). Cell lysate from human umbilical vein endothelial cells, which do not express LRP1, was used as a negative control (Figure 3.7B). We could not perform double staining of LRP1 and KIF13B in fibroblasts to analyze their colocalization due to the weak reactivity of our polyclonal antibody against the N-terminus of KIF13B, as described above.

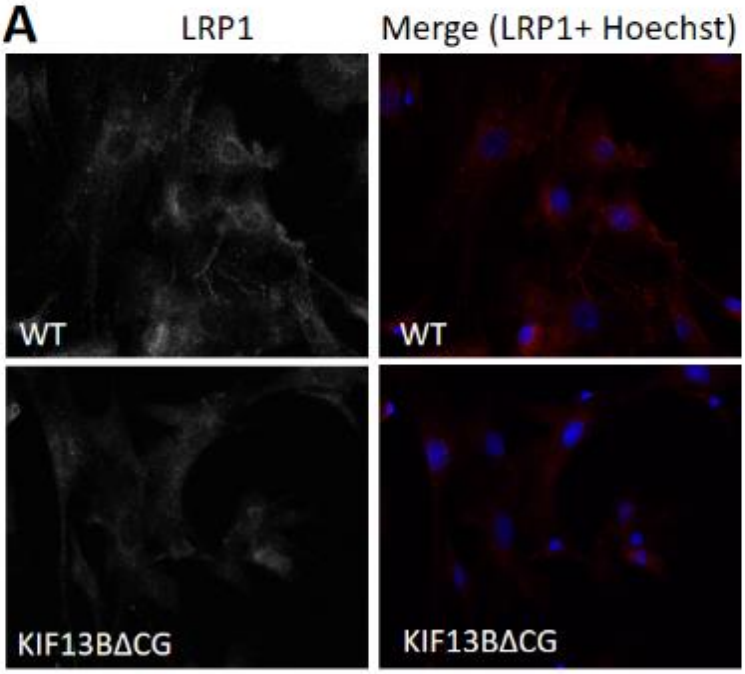

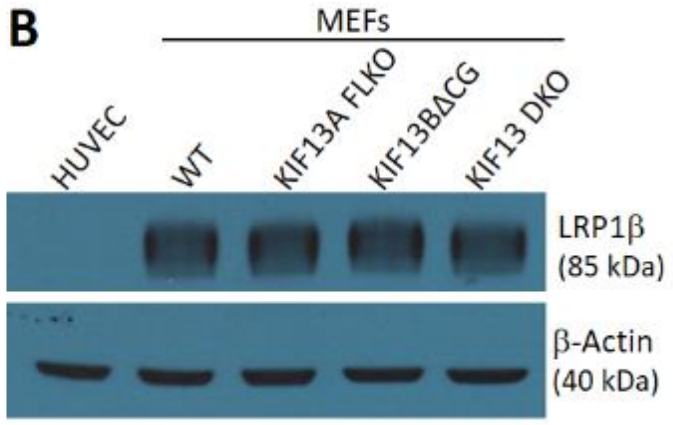

Figure 3.7. LRP1 subcellular localization and expression in MEFs. A) LRP1 subcellular localization in MEFs. MEFs were stained with LRP1 (red) and nuclear counterstain with Hoechst (blue). Pictures were taken at 40x and a representative frame was enlarged. B) LRP1 steady state protein expression in MEFs by Western blotting. Human umbilical vein endothelial cells served as the negative control for LRP1 expression, and β-actin was used as a loading control.

3.2.2. Biotinylation of surface LRP1

Since our results demonstrated that the steady state expression of LRP1 protein is similar in WT and KIF13BΔCG MEFs, we further investigated the subcellular localization of LRP1 in these MEFs. To investigate if LRP1 was trapped on the surface of the KIF13BΔCG MEFs due to reduced endocytosis caused by the CAP-Gly mutation in KIF13B, surface proteins of WT and KIF13BΔCG MEFs were biotinylated and precipitated from complete lysates with Neutravidin beads. The eluents from the beads were separated by SDS-PAGE and blotted with Streptavidin-HRP to confirm biotinylation and purification. As shown in Figure 3.8A, there was successful biotinylation (Input lanes + Biotin), and the labeled proteins were successfully purified with the beads (Beads lanes + Biotin). The selective biotinylation of surface proteins was confirmed by the absence of β-actin on the beads, which is only found in the cytoplasm (Figure 3.8B). Unfortunately, we encountered technical challenges when analyzing the surface LRP1. Only a minimal amount of surface LRP1 was accessible to biotinylation and pulled out with the beads. Moreover, our surface protein positive control, the Na^+/K^+ ATPase, was not detectable in either the Beads or Input lanes. This control was required as a loading control to normalize the surface LRP1 protein. Without a reliable antibody for our positive control and our low yield of surface LRP1, this experimental approach was not pursued further.

3.3 Cloning, expression, and protein interaction assays

Using tagged protein constructs and immunofluorescence microscopy, Kanai and colleagues have recently shown that hDLG1 serves as an adaptor between LRP1 and KIF13B at the membrane (24). To further expand our understanding of how KIF13B could be regulating LRP1, we investigated the protein-protein interactions of this complex. A

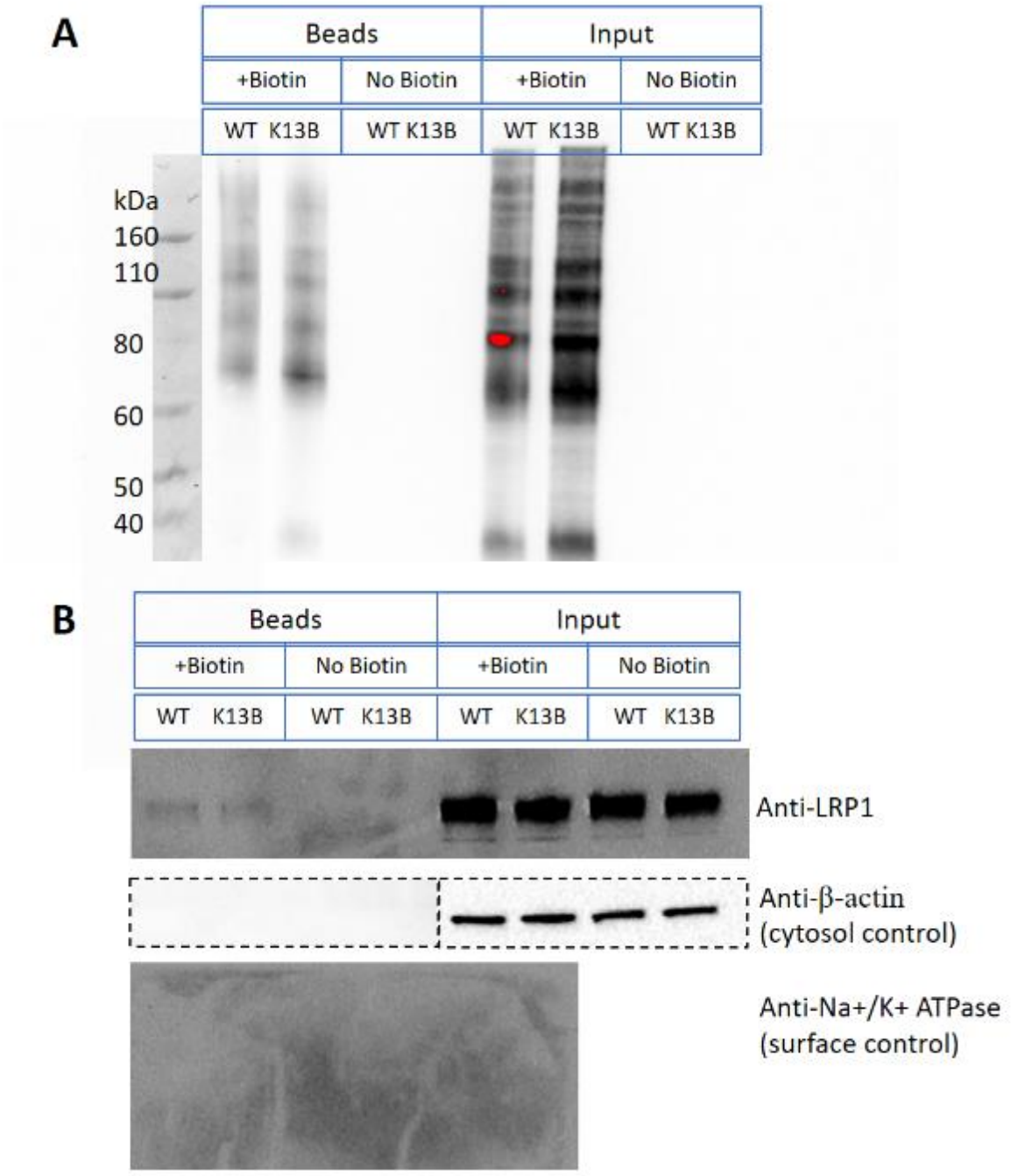

Figure 3.8. Surface LRP1 biotinylation. A) Streptavidin-HRP blot to confirm biotinylation of only surface proteins in MEFs from WT and KIF13BΔCG mice. B) Western blot for surface LRP1. β-actin was used as a cytosolic fraction control and Na^+/K^+ ATPase was attempted as a surface protein loading control. The β-actin membrane was excised from the same membrane as the LRP1 blot. The β-actin boxes show two different exposures, the input blot was exposed for 1 second, the Beads blot was exposed for 200 seconds. The Na^+/K^+ ATPase blot includes the same samples (without "No Biotin Input" samples) but analyzed on a different gel.

detailed characterization of the ternary complex between LRP1-hDLG1- KIF13B is required since many transmembrane proteins are known to recognize hDLG1 via its PDZ domains (64). In fact, the previous study by Kanai and colleagues implied that this possibility may indeed be the case for LRP1 recognition of hDLG1. Their data using a dominant negative construct of hDLG1, which is a GFP-tagged construct that includes only the SH3-I_3-GUK domains, shows colocalization only with their myc-KIF13B protein but not LRP1 (24).

3.3.1. TRX-LRP1 cloning and purification

Generation of a tagged LRP1 protein expressing a functional cytoplasmic domain was the most straightforward approach to investigate LRP1's interaction with hDLG1. Since LRP1 is a Type I transmembrane protein with a 100-amino acid cytoplasmic domain, we generated a TRX-tagged LRP1-cytoplasmic domain construct termed TRX-LRP1-CT. This construct was made by generating a PCR product of the CT with added restriction enzymes sites using LRP1-Herz as a template: BamHI at the 5' end and EcoRV at the 3' end (Primers 2 and 3 in Figure 3.9A). The digested PCR products of LRP1-CT with added restriction enzyme sites (Figure 3.9B, left green circle) were ligated into a digested pET32a backbone. Positive clones were identified by PCR using the TRX forward primer and LRP1 reverse primer (Figure 3.9C top, green circle). Sequencing was performed to confirm proper insertion into the backbone. We also attempted to create a TRX-LRP1-Herz construct in the same manner, using primer 1 from Figure 3.9A. After multiple attempts, a positive clone was identified (Figure 3.9C bottom, green circle); however, sequencing revealed inappropriate insertion, and therefore this approach was abandoned.

The expression of the TRX-LRP1-CT protein was induced by IPTG in BL21 *E. coli* and purified via FPLC on a NiNTA column. Fractions were collected every two minutes over 20 minutes (Figure 3.10A bottom, hash marks on X-axis). To confirm the presence and purity of the protein, fractions 3-10 were analyzed separately by SDS-PAGE and the gel was stained with Coomassie blue (Figure 3.10B bottom). Fractions 4-7 were pooled and used in the pull-down assays.

As a negative control for the pull-down assays, the TRX protein was expressed and purified in parallel to TRX-LRP1-CT. Fractions were collected every four minutes over 75 minutes (Figure 3.10A top, hash marks on X-axis), and fractions 5-12 were run on SDS-PAGE, and the gel was stained with Coomassie blue (Figure 3.10B top.) Fractions 6-10 were pooled and used in the pull-down assays.

Finally, to confirm the expression and identification by immunoblotting, the pooled fractions for both TRX and various dilutions of TRX-LRP1-CT were analyzed by SDS-PAGE alongside the protein from the uninduced (no IPTG) BL21 *E. coli*. One gel was stained with Coomassie blue and showed bands of appropriate size in only the induced lanes: TRX at ~25 kDa and TRX-LRP1-CT at ~35 kDa (Figure 3.10C top left). Another gel was transferred to a nitrocellulose membrane and stained with Ponceau S (Figure 3.10C top right), and then immunoblotted with a TRX antibody. Both TRX and TRX-LRP1-CT bands were identified by the TRX antibody, with TRX showing an additional band ~50 kDa that represents the commonly observed dimer species. As expected, the TRX-LRP1-CT fusion showed an increasing intensity with decreasing dilution (Figure 3.10C bottom.)

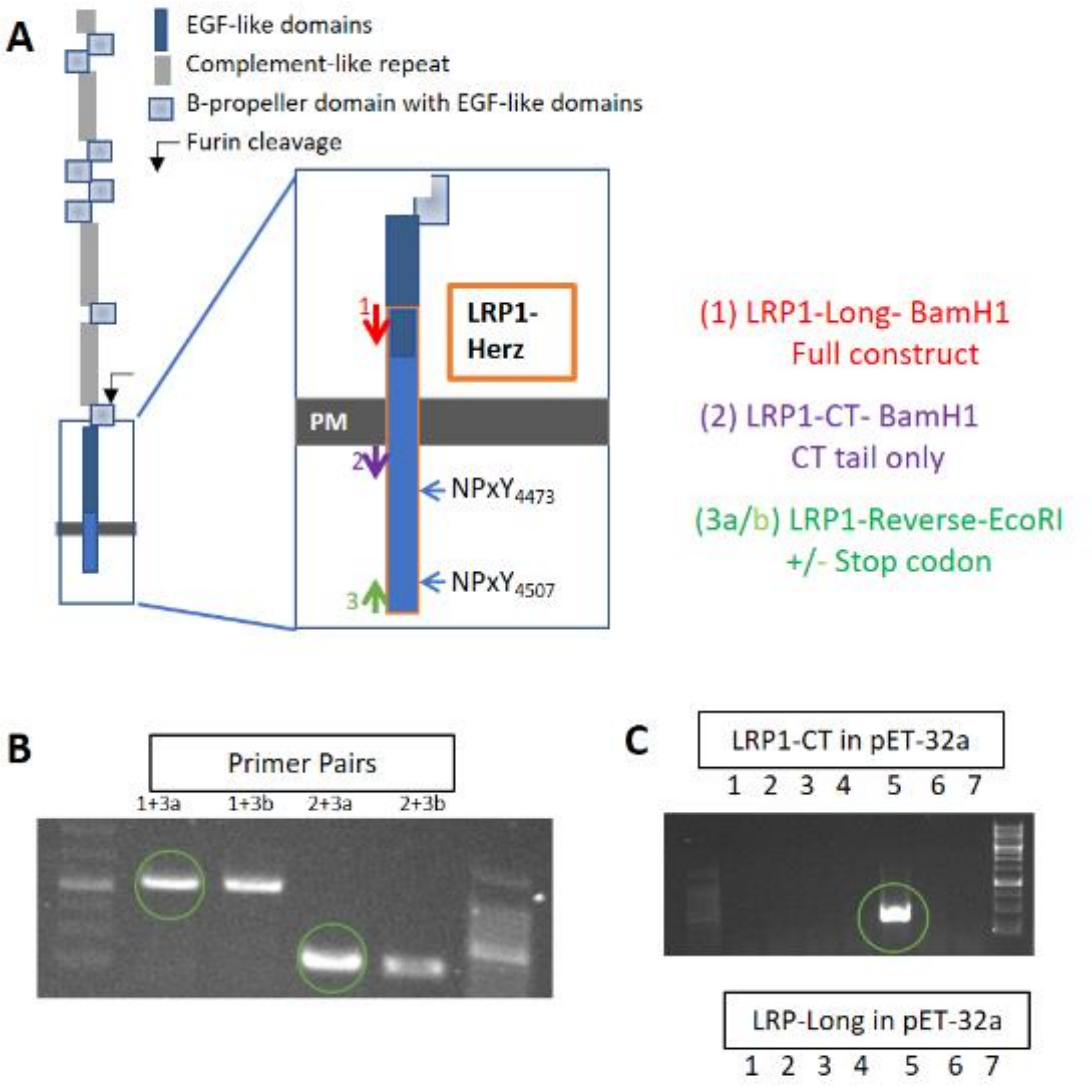

Figure 3.9. LRP1 constructs and primer designs. A) Cartoon of LRP1. Window magnifies LRP1-β to identify LRP1-Herz construct, primer targets for cloning, and NPxY domains in the cytoplasmic tail, in which Y4507 is mutated to LRP1-Y4507F. Orange box= Herz construct, Red arrow 1= forward primer for LRP1-Long sequence with BamHI site added (start of Herz construct), Purple arrow 2= forward primer for LRP1-CT with BamHI site added (cytoplasmic tail starting at first nucleotide after transmembrane domain), and Green arrow 3= reverse primer (a) with or (b) without the stop codon with EcoRV site added. PM= plasma membrane. B) PCR products using indicated primers and LRP1-Herz as a template. Products in lane 1 and 3 (green circle) were used to ligate into the pET-32a(+) backbone to add a TRX tag. C) PCR of clones with successful insertion of LRP1-CT (top, lane 5) and LRP1-Long (bottom, lane 7) using TRX forward primer and LRP1(a) reverse primer.

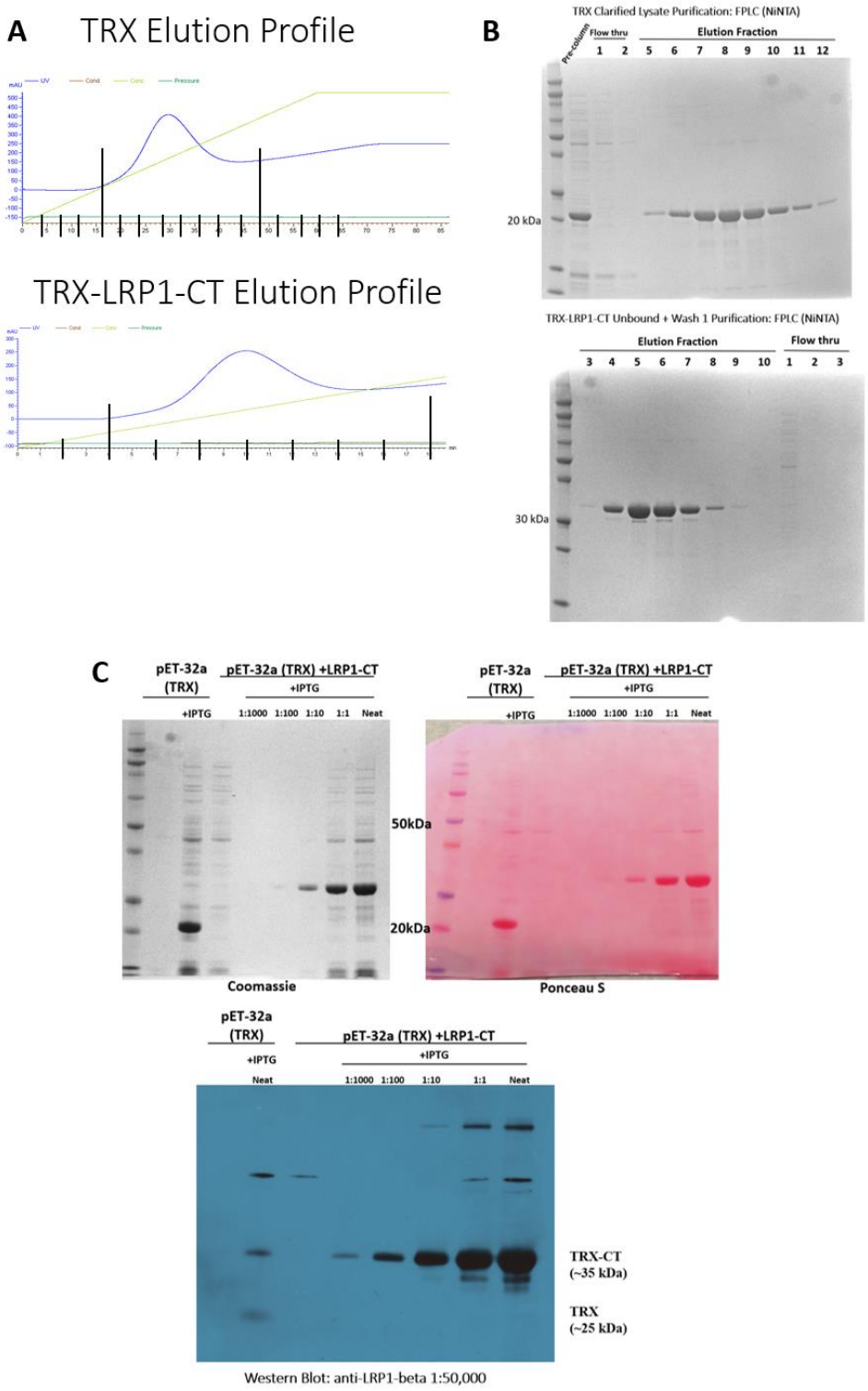

Figure 3.10. Purification, expression, and verification of TRX tagged LRP1-CT. A) Elution profile of NiNTA column. B) Coomassie stain of eluted fractions of TRX (top) and TRX-LRP1-CT (bottom). C) Coomassie, Ponceau S, and Western blot to confirm TRX and TRX-LRP1-CT induced expression in BL21 *E. coli*.

3.3.2. LRP1 interacts with the I_3 domain of hDLG1

To investigate the biochemical basis of LRP1-hDLG1 interaction, we employed a series of defined fusion proteins of hDLG1 and pull-down assays (Figure 3.11 and 3.12). Several hDLG1 constructs expressed as GST fusion proteins (Figure 3.11A & B) were used to pull-down the purified TRX-LRP1-CT protein expressed in bacteria. None of the hDLG1 segments was successful in demonstrating LRP1-hDLG1 interaction (Figure 3.12A). This unexpected observation suggested that lack of direct binding between LRP1 and hDLG1 under these conditions could be due to either post-translational modifications lacking in the bacterially expressed LRP1-CT protein or its improper folding due to some missing co-factors (51). A successful construction of active TRX-LRP1-Herz fusion protein would be useful to test the feasibility of LRP1-hDLG1 interaction.

As an alternative strategy, we used a construct gifted from the Herz lab to express a longer segment of LRP1 in a mammalian expression system for the binding studies. This construct, designated LRP1-Herz, includes the cytoplasmic tail of LRP1 as well as the transmembrane domain and part of the extracellular domain that includes six extracellular EGF-like domains of LRP1. This construct produced a protein smaller than the full β subunit by about 30 kDa (229 extracellular amino acids in LRP1-Herz versus 457 extracellular amino acid in LRP1β (57)) (Figure 3.9A). LRP1-Herz was transfected into HEK293T cells and total lysates from 24-hour post-transfection cells were used as prey. The GST-hDLG1 fusion proteins were used as bait in the pull-down assays (Figure. 3.11A & B). The hDLG1 constructs that included the alternatively spliced I_3 insertion, but not the I_2 insertion, successfully pulled down the LPR1-Herz protein expressed in HEK293T cell

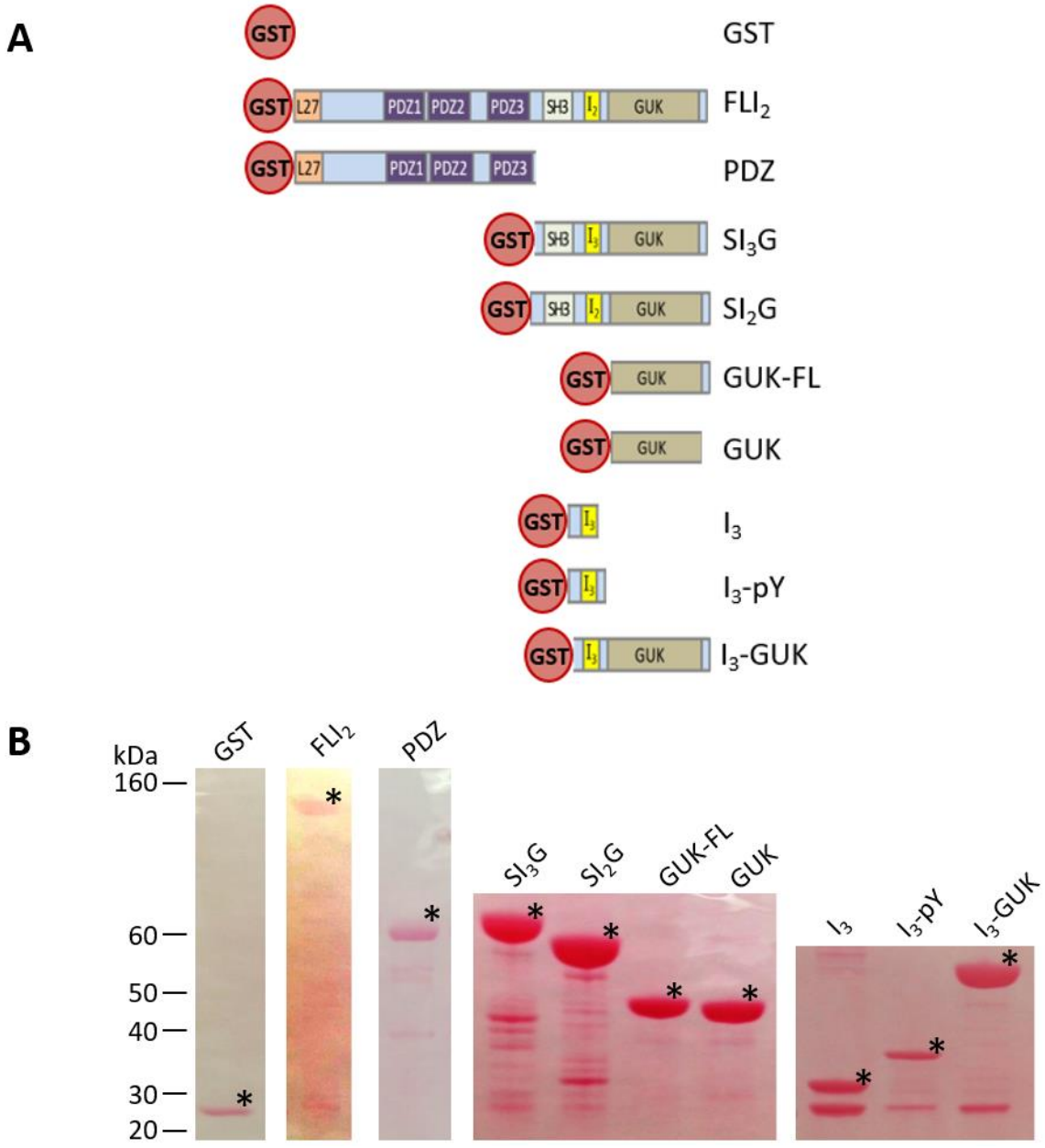

Figure 3.11. GST constructs used for pull-down assays. A) Cartoons of GST-tagged hDLG1 constructs used in the pull-down assays. GST = tag only, FLI_2 = full length hDLG1 with Insert 2, PDZ = PDZ 1-3 domains, SI_3G = SH3-Insert 3-GUK domains, SI_2G = SH3-Insert 2-GUK domains, GUK = GUK domain, GUK-FL = GUK domain and C-terminus, I_3 = Insert 3 only, I_3-pY = full I_3 insert with pY segment, I_3-GUK = Insert 3-GUK domains. All constructs have the GST tag. B) Ponceau staining of the membrane shows verification of protein expression of each GST construct (marked with *).

lysates (Figure. 3.12B). An important requirement was the presence of the GUK domain in the active hDLG1 constructs for binding to the LPR1-Herz protein. The GUK domain alone did not bind to LPR1-Herz protein (Figure. 3.12B). This finding suggests that the GUK domain confers stability to the relatively small 34 amino acid I_3 sequence that would be otherwise exposed, unstructured, and prone to degradation. Consistent with this model, the GST-I_3 construct without the GUK domain did not bind to LRP1-Herz protein (Figure. 3.12B). Finally, a comparison of SH3-I_2-GUK and SH3-I_3-GUK constructs confirmed that the I_3 sequence of hDLG1 is critical for binding to the cytoplasmic domain of LRP1 (Figure. 3.12B).

3.3.3. Effect of tyrosine phosphorylation of LRP1 on hDLG1 interaction

The two NPxY motifs in the cytoplasmic tail of LRP1 serve as sites of regulation for adaptor protein interactions. Phosphorylation of the tyrosine residues at Y4507 and Y4473 located within these NPxY motifs have been shown to regulate various interactions of LRP1 with adaptor proteins (51-53). To investigate if the hDLG1 interaction with LRP1 is regulated by the phosphorylation of Y4507, we replaced the Y4507 in LRP1-Herz construct with phenylalanine. This construct termed LRP1-Y4507F, which acts as a phospho-dead mutation, retains the aromatic ring with no impact on protein expression. The SH3-I_3-GUK construct of hDLG1 successfully pulled down both LRP1-Herz and LRP1-Y4507F constructs (Figure. 3.12C) indicating that loss of tyrosine phosphorylation of LRP1-CT does not affect its interaction with hDLG1. In fact, upon equal protein loading (Figure 3.12C bottom), a semi-quantitative assessment of the LRP1-hDLG1 interaction suggests that the mutation of Y4507 to phenylalanine in LRP1-CT may in fact potentiate the LRP1-hDLG1 interaction under these conditions. To validate this observation,

mutating Y4507 to glutamic acid to act as a phospho-mimetic and repeat the pull-down assays would be necessary.

3.3.4. Existence of endogenous LRP1 and hDLG1 complex

To further investigate the physiological relevance of the LRP1/hDLG1/KIF13B complex, we performed co-immunoprecipitation experiments using HepG2 human liver cell line that expresses both LRP1 and KIF13B. Endogenous LRP1 was co-precipitated with hDLG1 from the detergent solubilized membrane fraction using a monoclonal antibody 2D11 directed against the N-terminus of hDLG1 (Figure 3.12D). This result demonstrates the existence of an endogenous interaction between LRP1 and hDLG1 in these cells. We could not detect LRP1 in the immunoprecipitate of anti-KIF13B using a monoclonal antibody 4A5 directed against the C-terminus of human KIF13B. This observation might reflect the transient nature of interaction of the KIF13B motor with LRP1/hDLG1 complex in this cell line. Since the interaction between hDLG1 and KIF13B has been well established (4), it is likely that LRP1, hDLG1, and KIF13B form a stable ternary complex in the polarized hepatocytes harvested as primary cells from liver. Our attempt to detect hDLG1 in the immunoprecipitate of LRP1 was also unsuccessful presumably because the binding of the LRP1 monoclonal antibody occluded hDLG1 interaction within the short stretch of LRP1 cytoplasmic domain.

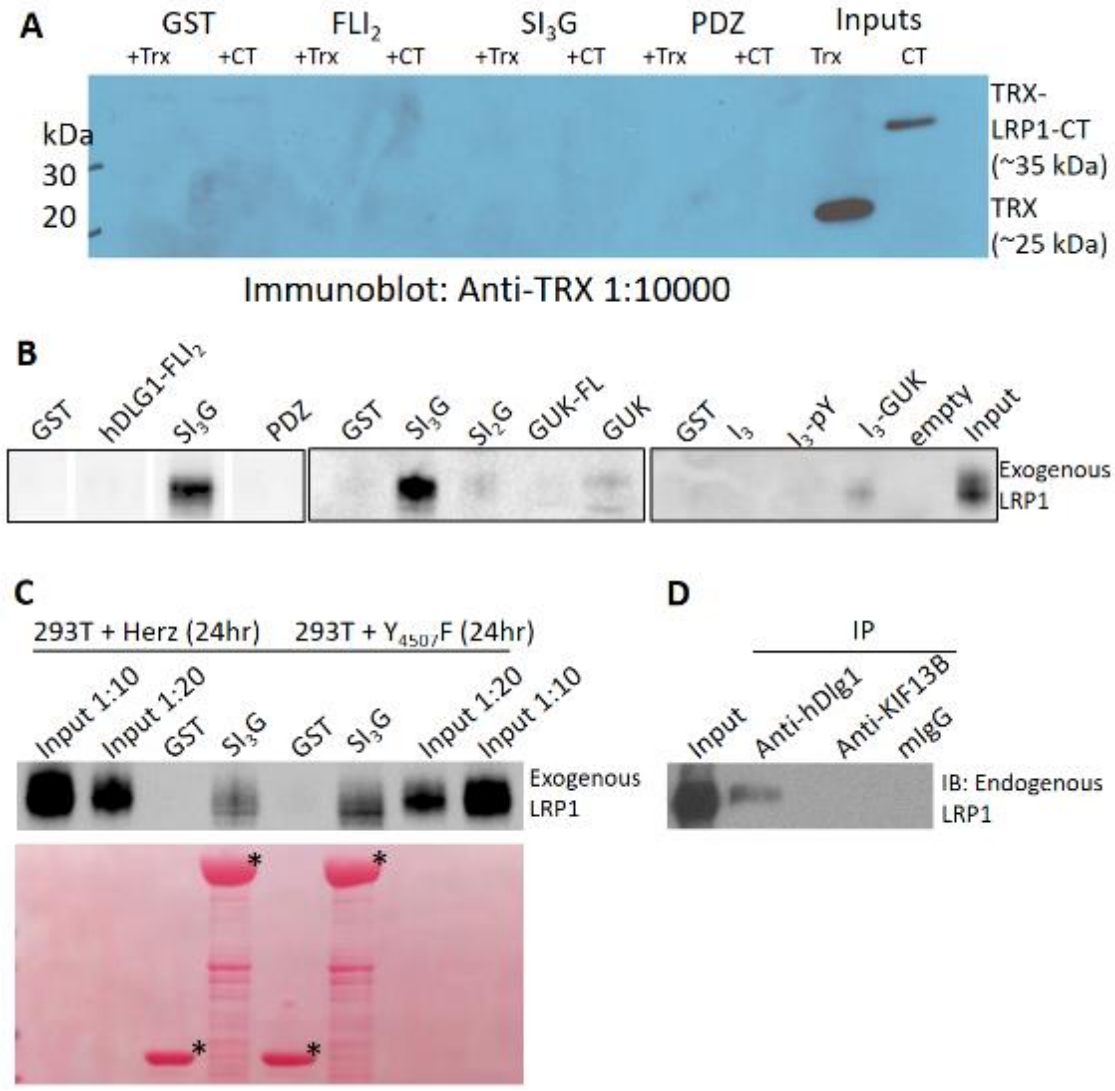

Figure 3.12. Protein interaction assays. A) Immunoblot of TRX-LRP1-CT in pull-down assays. The GST constructs (bold, top) were used as bait and purified TRX or TRX-LRP1-CT protein was the targeted prey. Anti-TRX antibody was used for immunoblotting. B) Immunoblot of LRP1-Herz in pull-down assays from transfected HEK293T cell lysates. Anti-LRP1 antibody was used for immunoblotting and identified exogenous LRP1-β in the input lane and in the lanes corresponding to the beads that contain the I_3 domain of hDLG1. Each box represents a different gel and breaks indicate non-consecutive wells. C) Immunoblot of LRP1-Herz or LRP1-Y4507F in pull-down assays from transfected HEK293T cell lysates. LRP1 antibody identified exogenous LRP1-β in the input lane and in the lanes corresponding to the beads that contain the I_3 domain of hDLG1. Ponceau staining of the membrane verifies GST construct expression (marked with *) and equal loading of protein onto glutathione S beads. D) Co-IP of LRP1 by anti-hDLG1, anti-KIF13B, or mouse IgG in the membrane fraction of HepG2 lysates.

Chapter 4: DISCUSSION

This study reports the first characterization of a mouse model expressing a truncated form of KIF13B specifically lacking its CAP-Gly domain. We showed the CAP-Gly domain of KIF13B is important for stabilization and proper localization of the protein. The mislocalization of KIF13B perhaps renders the protein non-functional, which is why it has a similar phenotype to KIF13B FLKO mice in regard to elevated blood cholesterol (24). Additionally, we discovered that the I_3 insert of hDLG1 is necessary for the interaction with the cytoplasmic tail of LRP1, contrary to the speculation that the PDZ domains of hDLG1 would be the necessary domains for this interaction. Finally, we were surprised to find that the mutation of Y4507 to a phospho-dead phenylalanine seems to enhance the interaction between hDLG1 and LRP1.

Mammalian kinesins are grouped into 15 families encompassing 45 motor proteins (1). The kinesin-3 family includes 8 members including two homologs termed KIF13A and KIF13B. Among the 45 known kinesins, the KIF13B is the only motor that contains a CAP-Gly domain at its C-terminus. We used our mouse model with a truncated KIF13B protein that lacks the CAP-Gly domain to investigate its role in LRP1 endocytosis. In addition, KIF13A FLKO mice were used to assess any compensatory role. Unlike KIF13B, KIF13A lacks a CAP-Gly domain and does not bind to hDLG1 (Hanada, unpublished data). Recently, Hirokawa and colleagues reported a functional role of KIF13B in the endocytosis of LRP1 (24). Using a KIF13B FLKO mouse model, they demonstrated ~25% elevation of serum cholesterol and plasma factor VIII, which are known ligands of LRP1. Nonetheless, the increase in plasma factor VIII was heterogenous showing a large variation in 10 animals analyzed in their study (24). Unlike KIF13B FLKO mice, our mouse model

only lacks the CAP-Gly domain of KIF13B thus permitting specific evaluation of its function *in vivo*. Our findings demonstrated an increase in the serum lipoprotein levels in KIF13BΔCG mice, a phenotype that is similar to KIF13B FLKO mice (24). The total cholesterol levels in our WT mice had a slightly elevated mean and larger standard error of mean (SEM) compared to previously reported levels in C57BL6 mice (24), which may obscure the true significance compared to the KIF13BΔCG levels. Furthermore, the LDL levels in mice are inherently low because they rely more on HDL, rather than LDL, to traffic cholesterol through their bodies. Therefore, what seems like a small increase in LDL levels in the KIF13BΔCG mice is truly significant. The KIF13A FLKO mice did not show any functional effect on serum cholesterol. Conversely, our measurements of plasma factor VIII by two independent assays did not show any statistically significant elevation in KIF13BΔCG mice. This finding suggests that either the CAP-Gly domain of KIF13B differentially regulates the endocytosis of LRP1 ligands or the variation in factor VIII levels requires further validation of this phenotype in a larger number of age and sex matched animals. Alternatively, the CAP-Gly domain may have a role in the endocytosis of other receptors that recognize LDL, and while the Kanai paper ruled out the involvement of the LDL receptor (24), there are other family members that have yet to be investigated.

To investigate the biochemical basis of lipid homeostasis in mutant mice, we measured the uptake of LDL in fibroblasts generated from the KIF13BΔCG and found it was slightly reduced as compared to wild-type mice. The hydrolysis of LDL-derived cholesterol esters was unaffected by the KIF13B truncation. Furthermore, LDL stimulation of cholesterol esterification was also unaffected in the KIF13ΔCG MEFs as compared to the wild-type, demonstrating that the trafficking of cholesterol from lysosomes to the

endoplasmic reticulum is normal, as well as the esterification machinery in the endoplasmic reticulum. These findings suggest a functional role of the CAP-Gly domain in only the endocytosis element of this trafficking pathway, using lipoproteins as our ligand to measure these aspects of endocytosis. We also examined the expression of KIF13BΔCG protein in brain sections and found that the truncated protein exhibits lower expression and altered subcellular localization as compared to the WT protein. These findings suggest that the CAP-Gly domain plays a role in the stabilization and appropriate localization of KIF13B.

Moreover, we found altered subcellular localization of LRP1 in KIF13BΔCG MEFs as compared to WT mice. Since Western blotting did not show any change in the steady state levels of LRP1 across genotypes, altered LRP1 immuno-localization is presumably due to the mislocalization of the receptor. The lack of efficient endocytosis of LRP1 ligands could be attributed to the accumulation of surface LRP1 by the deletion of CAP-Gly domain of KIF13B. To interrogate this possibility, we attempted to quantify the amount of surface LRP1 in fibroblasts using surface protein biotinylation approach. However, only a minimal amount of surface LRP1 was able to be biotinylated and pulled out with the beads. This is likely due to the large extracellular α subunit of LRP1 masking the extracellular domain of the β subunit. The α subunit is likely a "sink" for the biotin, and that subunit cannot be blotted for due to its large size and unstable non-covalent bond to the β subunit. A semiquantitative analysis shows the levels of biotinylated surface LRP1β do not seem to differ between the various MEFs; however, our surface protein positive control, the Na^+/K^+ ATPase, was not detectable in any of our samples using the available antibody. This control is necessary to 1) confirm appropriate technique conditions and 2) to use as a loading control to normalize our surface LRP1 protein to, as there is no

indication that the levels of this protein should be altered between these MEFs. Without a reliable antibody for our positive control and our low yield of surface LRP1, this experiment was abandoned. Moving forward, the precise location of LRP1 in KIF13BΔCG fibroblasts should be investigated using organelle-specific probes with LRP1 staining in conjunction with high resolution microscopy.

Since LRP1 does not bind to KIF13B directly, Kanai *et al* proposed that hDLG1 may function as an adaptor to link LRP1 with KIF13B (24). In their study, disruption of LRP1 localization in fibroblasts using a dominant negative mutant of hDLG1 (GFP-hDLG1-DN), which is a GFP-tagged construct that includes only the SH3-I_3-GUK domains and colocalizes with their myc-KIF13B protein but not LRP1, implied that LRP1 may bind to the amino terminal half of hDLG1 (24). This model seems to be consistent with the premise that the C-termini of multiple transmembrane proteins recognize the PDZ domains of adaptor proteins (reviewed in (65)). Since hDLG1 contains three PDZ domains in its N-terminal half, we tested the LRP1-hDLG1 interaction using pull-down assays. Our first attempt using purified TRX-LRP1-CT in a bacterial system did not reveal any interactions with the hDLG1 constructs, which suggests 1) the TRX-LRP1-CT protein was too small and unstructured for the interaction to take place, 2) post-translational modification of LRP1-CT is necessary for this interaction, or 3) other proteins are involved in this complex.

Our next approach to the protein-protein interaction investigation shifted into a mammalian system. The LRP1 construct composed of the CT, transmembrane domain, and part of the extracellular domain (LRP1-Herz) expressed in a mammalian system did not bind to the three PDZ domains of hDLG1 as expected. However, further scanning of other

hDLG1 domains revealed that LRP1-Herz specifically recognizes the I_3 domain of hDLG1. Previous studies have shown that the alternatively spliced I_3 motif, flanked by the SH3 and GUK domains in hDLG1, binds to the FERM domain of protein 4.1 family of cytoskeletal proteins (36). In addition, we have demonstrated that the SH3-I_3-GUK, but not SH3-I_2-GUK, module of hDLG1 activates the microtubule-stimulated ATPase activity of KIF13B by 10-fold (10). Genetic studies of *Drosophila* discs large tumor suppressor protein (DLG1) have shown that the HOOK domain, which corresponds to the I_3 motif in hDLG1, is essential for maintaining the epithelial structure and growth regulation (33). This observation is consistent with the previous findings that the I_3 motif plays a critical role in recruiting hDLG1 to the plasma membrane of epithelial cells (36).

Kanai *et al* has shown that their myc-KIF13B and GFP-hDLG1-DN proteins colocalize when over-expressed in KIF13B FLKO MEFs; however, this complex fails to colocalize with endogenous LRP1 (24). On the other hand, we have shown the LRP1 interacts with hDLG1 via the I_3 domain of hDLG1, which is present in Kanai's GFP-hDLG1-DN. There are a couple of possible explanations of why the myc-KIF13B and GFP-hDLG1-DN complex did not colocalize with LRP1, even with the I_3 of hDLG1 present. First, GFP-hDLG1-DN is missing a large amount of the protein; therefore, this may render it, and the complex, non-functional, thus preventing the interaction with the cytoplasmic tail of LRP1. Additionally, endogenous hDLG1 was still being expressed in these MEFs, so the LRP1-hDLG1 interaction may still exist, and the GFP-hDLG1-DN protein could not out compete the endogenous hDLG1. Finally, the use of over-expressed, tagged proteins may have a preferential binding to each other, yielding a complex unable to be properly localized to the cytoplasmic tail of LRP1 (24). What was not reported was

if LRP1 and GFP-hDLG1-DN colocalized; this may be helpful in addressing if this interaction exists in an over-expression model.

LRP1 is detected as a broad band in Western blots because of its numerous post-translational modifications. When LRP1 was coimmunoprecipitated with hDLG1 from HepG2 lysates, the larger-sized fraction of total LRP1β was seen. This further observation further suggests the necessity of post-translational modification of LRP1 to allow interaction with hDLG1. To test if the LRP1-hDLG1 interaction is regulated by phosphorylation, we mutated the tyrosine 4507 to phenylalanine in the LRP1 cytoplasmic tail thus mimicking a phospho-dead mutation. Unexpectedly, we observed an enhancement of LRP1 interaction with hDLG1. To validate this observation, mutating Y4507 to glutamic acid to act as a phospho-mimetic and repeat the pull-down assays would be necessary. It is important to note, the mutation to glutamic acid is more suited to mimic phosphoserine or phosphothreonine. To validate Y4507E as an appropriate phosphotyrosine mimic, proper controls must be included, such as comparing to an alanine substitution in place of the tyrosine (66). Additionally, a complementary *in vivo* analysis of LRP1-hDLG1 interaction would be required to assess the biological significance of this observation. Together, these observations raise the possibility that the LRP1 interaction with the I_3 domain of hDLG1 may constitute a novel switch that regulates the cytoskeletal reorganization affecting the clustering and localization of receptors by KIF13B. Our model is detailed in Figure 4.1A.

LRP1's interaction with hDLG1 may have implications for non-endocytic signaling pathways. If the interaction with hDLG1, and thus KIF13B, is the preferential interaction over other adaptor proteins, without the formation of this complex in the KIF13ΔCG mice, there may be enhanced downstream signaling that would not otherwise be seen. In

particular, if hDLG1 does not interact with LRP1-CT, it can become more accessible to phosphorylation (40, 54), thus shifting the balance between LRP1 endocytosis and LRP1 signaling. Investigating the downstream targets of LRP1 signaling in wild-type and KIF13BΔCG systems would be an important next step to improve our understanding of LRP1 signaling regulation.

In summary, our findings demonstrate that KIF13B specifically lacking its CAP-Gly domain retains its motor activity and can translocate to the membrane when activated, as indicated by the movement of the protein to the leading edge in migrating MEFs (Figure 3.1E). However, the deletion of CAP-Gly results in the mislocalization of truncated KIF13B, thus preventing the dysfunctional KIF13B to regulate LRP1 endocytosis *in vivo* via hDLG1 (Figure 4.1B). The cytoplasmic tail of LRP1 interacts specifically with the alternatively spliced I_3 insert of hDLG1, and other post-translational modification of LRP1-CT likely play a regulatory role for this interaction; however, it is not due to the modification of Tyr4507. Using markers of KIF13A and KIF13B complexes, future characterization of these mouse models and the regulation of the interaction between LRP1-CT and hDLG1 are likely to enhance our mechanistic understanding of LRP1 endocytosis with implications in diseases such as hypercholesterolemia, tumorigenesis, thrombosis, and Alzheimer's disease.

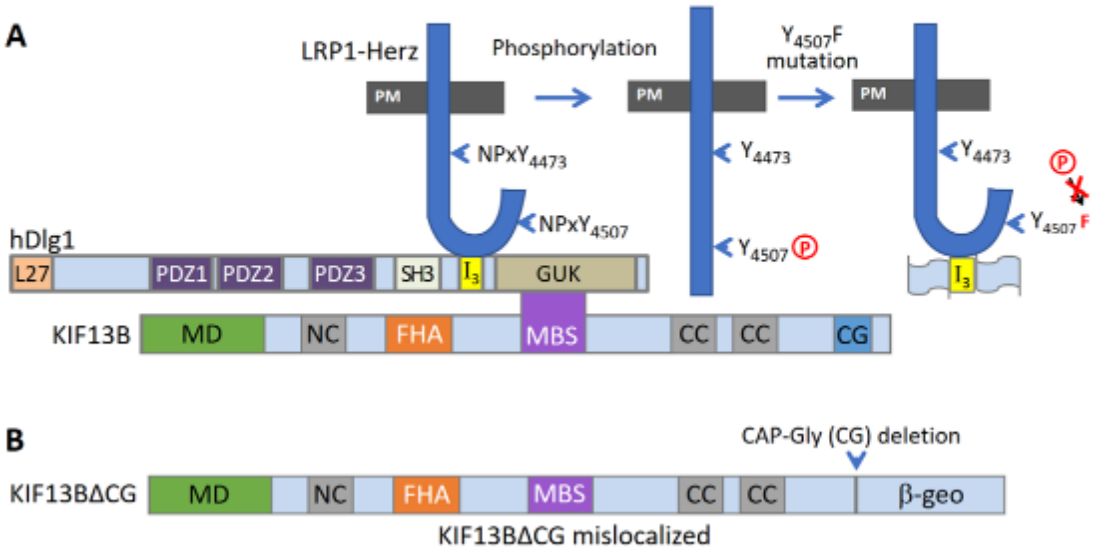

Figure 4.1. Proposed LRP1-hDLG1-KIF13B interaction model. A) hDLG1 interacts with LRP1-CT via its I_3 domain and with KIF13B's MBS domain via its GUK domain. When Y4507 of LRP1 is not phosphorylated, the shape of the cytoplasmic tail allows for interaction with hDLG1. Upon phosphorylation, the site of interaction is disrupted and decreases the strength of binding. When Y4507 is mutated into a phenylalanine, which cannot be phosphorylated, this causes the CT to retain a conformation that allows for optimal hDLG1 interaction. B) KIF13B interacts with LRP1-CT at the plasma membrane via hDLG1. Truncation of the CAP-Gly domain of KIF13B mislocalizes the protein away from the plasma membrane, preventing this complex from forming and efficiently inducing LRP1 endocytosis. The mislocalization of KIF13B leads to the mislocalization of LRP1.

Chapter 5: BIBLIOGRAPHY

1. Hirokawa N, Noda Y, Tanaka Y, Niwa S. Kinesin superfamily motor proteins and intracellular transport. Nat Rev Mol Cell Biol. 2009;10(10):682-96. doi: 10.1038/nrm2774. PubMed PMID: 19773780.
2. Nakagawa T, Setou M, Seog D, Ogasawara K, Dohmae N, Takio K, Hirokawa N. A novel motor, KIF13A, transports mannose-6-phosphate receptor to plasma membrane through direct interaction with AP-1 complex. Cell. 2000;103(4):569-81. PubMed PMID: 11106728.
3. Delevoye C, Hurbain I, Tenza D, Sibarita JB, Uzan-Gafsou S, Ohno H, Geerts WJ, Verkleij AJ, Salamero J, Marks MS, Raposo G. AP-1 and KIF13A coordinate endosomal sorting and positioning during melanosome biogenesis. The Journal of cell biology. 2009;187(2):247-64. doi: 10.1083/jcb.200907122. PubMed PMID: 19841138; PMCID: PMC2768840.
4. Hanada T, Lin L, Tibaldi EV, Reinherz EL, Chishti AH. GAKIN, a novel kinesin-like protein associates with the human homologue of the Drosophila discs large tumor suppressor in T lymphocytes. The Journal of biological chemistry. 2000;275(37):28774-84. doi: 10.1074/jbc.M000715200. PubMed PMID: 10859302.
5. Miki H, Setou M, Kaneshiro K, Hirokawa N. All kinesin superfamily protein, KIF, genes in mouse and human. Proc Natl Acad Sci U S A. 2001;98(13):7004-11. doi: 10.1073/pnas.111145398. PubMed PMID: 11416179; PMCID: PMC34614.
6. Soppina V, Norris SR, Dizaji AS, Kortus M, Veatch S, Peckham M, Verhey KJ. Dimerization of mammalian kinesin-3 motors results in superprocessive motion. Proc Natl Acad Sci U S A. 2014;111(15):5562-7. doi: 10.1073/pnas.1400759111. PubMed PMID: 24706892; PMCID: PMC3992690.
7. Horiguchi K, Hanada T, Fukui Y, Chishti AH. Transport of PIP3 by GAKIN, a kinesin-3 family protein, regulates neuronal cell polarity. The Journal of cell biology. 2006;174(3):425-36. doi: 10.1083/jcb.200604031. PubMed PMID: 16864656; PMCID: PMC2064238.
8. Venkateswarlu K, Hanada T, Chishti AH. Centaurin-alpha1 interacts directly with kinesin motor protein KIF13B. J Cell Sci. 2005;118(Pt 11):2471-84. Epub 2005/06/01. doi: 10.1242/jcs.02369. PubMed PMID: 15923660.
9. Asaba N, Hanada T, Takeuchi A, Chishti AH. Direct interaction with a kinesin-related motor mediates transport of mammalian discs large tumor suppressor homologue in epithelial cells. The Journal of biological chemistry. 2003;278(10):8395-400. doi: 10.1074/jbc.M210362200. PubMed PMID: 12496241.
10. Yamada KH, Hanada T, Chishti AH. The effector domain of human Dlg tumor suppressor acts as a switch that relieves autoinhibition of kinesin-3 motor GAKIN/KIF13B. Biochemistry. 2007;46(35):10039-45. doi: 10.1021/bi701169w. PubMed PMID: 17696365; PMCID: PMC2525504.
11. Siegrist SE, Doe CQ. Microtubule-Induced Pins/Gαi Cortical Polarity in Drosophila Neuroblasts. Cell. 2005;123(7):1323-35. doi: https://doi.org/10.1016/j.cell.2005.09.043.
12. Lu Michelle S, Prehoda Kenneth E. A NudE/14-3-3 Pathway Coordinates Dynein and the Kinesin Khc73 to Position the Mitotic Spindle. Developmental Cell.26(4):369-80. doi: 10.1016/j.devcel.2013.07.021.

13. Monteiro MI, Ahlawat S, Kowalski JR, Malkin E, Koushika SP, Juo P. The kinesin-3 family motor KLP-4 regulates anterograde trafficking of GLR-1 glutamate receptors in the ventral nerve cord of Caenorhabditis elegans. Mol Biol Cell. 2012;23(18):3647-62. Epub 2012/08/03. doi: 10.1091/mbc.E12-04-0334. PubMed PMID: 22855524; PMCID: PMC3442412.
14. Steinmetz MO, Akhmanova A. Capturing protein tails by CAP-Gly domains. Trends in Biochemical Sciences.33(11):535-45. doi: 10.1016/j.tibs.2008.08.006.
15. Ayloo S, Lazarus JE, Dodda A, Tokito M, Ostap EM, Holzbaur EL. Dynactin functions as both a dynamic tether and brake during dynein-driven motility. Nature communications. 2014;5:4807. Epub 2014/09/05. doi: 10.1038/ncomms5807. PubMed PMID: 25185702; PMCID: PMC4470572.
16. Li S, Finley J, Liu Z-J, Qiu S-H, Chen H, Luan C-H, Carson M, Tsao J, Johnson D, Lin G, Zhao J, Thomas W, Nagy LA, Sha B, DeLucas LJ, Wang B-C, Luo M. Crystal Structure of the Cytoskeleton-associated Protein Glycine-rich (CAP-Gly) Domain. Journal of Biological Chemistry. 2002;277(50):48596-601. doi: 10.1074/jbc.M208512200.
17. Yan S, Guo C, Hou G, Zhang H, Lu X, Williams JC, Polenova T. Atomic-resolution structure of the CAP-Gly domain of dynactin on polymeric microtubules determined by magic angle spinning NMR spectroscopy. Proc Natl Acad Sci U S A. 2015;112(47):14611-6. doi: 10.1073/pnas.1509852112. PubMed PMID: 26604305; PMCID: PMC4664305.
18. Yan S, Hou G, Schwieters CD, Ahmed S, Williams JC, Polenova T. Three-dimensional structure of CAP-gly domain of mammalian dynactin determined by magic angle spinning NMR spectroscopy: conformational plasticity and interactions with end-binding protein EB1. J Mol Biol. 2013;425(22):4249-66. doi: 10.1016/j.jmb.2013.04.027. PubMed PMID: 23648839; PMCID: PMC3812427.
19. Gao J, Huo L, Sun X, Liu M, Li D, Dong JT, Zhou J. The tumor suppressor CYLD regulates microtubule dynamics and plays a role in cell migration. The Journal of biological chemistry. 2008;283(14):8802-9. Epub 2008/01/29. doi: 10.1074/jbc.M708470200. PubMed PMID: 18222923.
20. Wickstrom SA, Masoumi KC, Khochbin S, Fassler R, Massoumi R. CYLD negatively regulates cell-cycle progression by inactivating HDAC6 and increasing the levels of acetylated tubulin. EMBO J. 2010;29(1):131-44. Epub 2009/11/07. doi: 10.1038/emboj.2009.317. PubMed PMID: 19893491; PMCID: PMC2775896.
21. Farrer MJ, Hulihan MM, Kachergus JM, Dächsel J, Stoessl AJ, Grantier LL, Calne S, Calne DB, Lechevalier B, Chapon F, Tsuboi Y, Yamada T, Gutmann L, Elibol B, Bhatia KP, Wider CW, Vilariño-Güell C, Ross OA, Brown LA, Castanedes-Casey M, Dickson DW, Wszolek ZK. DCTN1 mutations in Perry syndrome. Nature genetics. 2009;41(2):163-5. doi: 10.1038/ng.293. PubMed PMID: PMC2813485.
22. Mishima T, Koga S, Lin W-L, Kasanuki K, Castanedes-Casey M, Wszolek ZK, Oh SJ, Tsuboi Y, Dickson DW. Perry Syndrome: A Distinctive Type of TDP-43 Proteinopathy. Journal of Neuropathology & Experimental Neurology. 2017;76(8):676-82. doi: 10.1093/jnen/nlx049.
23. Bignell GR, Warren W, Seal S, Takahashi M, Rapley E, Barfoot R, Green H, Brown C, Biggs PJ, Lakhani SR, Jones C, Hansen J, Blair E, Hofmann B, Siebert R, Turner G, Evans DG, Schrander-Stumpel C, Beemer FA, van den Ouweland A, Halley D,

Delpech B, Cleveland MG, Leigh I, Leisti J, Rasmussen S, Wallace MR, Fenske C, Banerjee P, Oiso N, Chaggar R, Merrett S, Leonard N, Huber M, Hohl D, Chapman P, Burn J, Swift S, Smith A, Ashworth A, Stratton MR. Identification of the familial cylindromatosis tumour-suppressor gene. Nature Genetics. 2000;25:160. doi: 10.1038/76006.
24. Kanai Y, Wang D, Hirokawa N. KIF13B enhances the endocytosis of LRP1 by recruiting LRP1 to caveolae. The Journal of cell biology. 2014;204(3):395-408. doi: 10.1083/jcb.201309066. PubMed PMID: 24469637; PMCID: PMC3912526.
25. Ramirez-Sanchez I, Mendoza-Lorenzo P, Zentella-Dehesa A, Mendez-Bolaina E, Lara-Padilla E, Ceballos-Reyes G, Canto P, Palma-Flores C, Coral-Vazquez RM. Caveolae and non-caveolae lipid raft microdomains of human umbilical vein endothelial cells contain utrophin-associated protein complexes. Biochimie. 2012;94(9):1884-90. Epub 2012/05/23. doi: 10.1016/j.biochi.2012.05.001. PubMed PMID: 22609462.
26. Sotgia F, Lee JK, Das K, Bedford M, Petrucci TC, Macioce P, Sargiacomo M, Bricarelli FD, Minetti C, Sudol M, Lisanti MP. Caveolin-3 directly interacts with the C-terminal tail of beta -dystroglycan. Identification of a central WW-like domain within caveolin family members. The Journal of biological chemistry. 2000;275(48):38048-58. Epub 2000/09/16. doi: 10.1074/jbc.M005321200. PubMed PMID: 10988290.
27. Ilsley JL, Sudol M, Winder SJ. The WW domain: linking cell signalling to the membrane cytoskeleton. Cell Signal. 2002;14(3):183-9. Epub 2002/01/29. PubMed PMID: 11812645.
28. Woods DF, Bryant PJ. Molecular cloning of the lethal(1)discs large-1 oncogene of Drosophila. Developmental biology. 1989;134(1):222-35. doi: https://doi.org/10.1016/0012-1606(89)90092-4.
29. Roberts S, Delury C, Marsh E. The PDZ protein discs-large (DLG): the 'Jekyll and Hyde' of the epithelial polarity proteins. FEBS J. 2012;279(19):3549-58. Epub 2012/08/01. doi: 10.1111/j.1742-4658.2012.08729.x. PubMed PMID: 22846345.
30. Caruana G, Bernstein A. Craniofacial Dysmorphogenesis Including Cleft Palate in Mice with an Insertional Mutation in the discs large Gene. Molecular and Cellular Biology. 2001;21(5):1475-83. doi: 10.1128/mcb.21.5.1475-1483.2001.
31. Mahoney ZX, Sammut B, Xavier RJ, Cunningham J, Go G, Brim KL, Stappenbeck TS, Miner JH, Swat W. Discs-large homolog 1 regulates smooth muscle orientation in the mouse ureter. Proc Natl Acad Sci U S A. 2006;103(52):19872-7. Epub 2006/12/19. doi: 10.1073/pnas.0609326103. PubMed PMID: 17172448; PMCID: PMC1750896.
32. Zhu J, Shang Y, Chen J, Zhang M. Structure and function of the guanylate kinase-like domain of the MAGUK family scaffold proteins. Frontiers in Biology. 2012;7(5):379-96. doi: 10.1007/s11515-012-1244-9.
33. Hough CD, Woods DF, Park S, Bryant PJ. Organizing a functional junctional complex requires specific domains of the Drosophila MAGUK Discs large. Genes Dev. 1997;11(23):3242-53. Epub 1998/02/12. PubMed PMID: 9389655; PMCID: PMC316757.
34. Wu H, Reissner C, Kuhlendahl S, Coblentz B, Reuver S, Kindler S, Gundelfinger ED, Garner CC. Intramolecular interactions regulate SAP97 binding to GKAP. The EMBO Journal. 2000;19(21):5740.

35. Lue RA, Marfatia SM, Branton D, Chishti AH. Cloning and characterization of hdlg: the human homologue of the Drosophila discs large tumor suppressor binds to protein 4.1. Proc Natl Acad Sci U S A. 1994;91(21):9818-22. Epub 1994/10/11. PubMed PMID: 7937897; PMCID: PMC44908.
36. Hanada T, Takeuchi A, Sondarva G, Chishti AH. Protein 4.1-mediated membrane targeting of human discs large in epithelial cells. The Journal of biological chemistry. 2003;278(36):34445-50. Epub 2003/06/17. doi: 10.1074/jbc.M305209200. PubMed PMID: 12807908.
37. Roberts S, Calautti E, Vanderweil S, Nguyen HO, Foley A, Baden HP, Viel A. Changes in localization of human discs large (hDlg) during keratinocyte differentiation is associated with expression of alternatively spliced hDlg variants. Experimental Cell Research. 2007;313(12):2521-30. doi: https://doi.org/10.1016/j.yexcr.2007.05.017.
38. Herz J, Kowal RC, Ho YK, Brown MS, Goldstein JL. Low density lipoprotein receptor-related protein mediates endocytosis of monoclonal antibodies in cultured cells and rabbit liver. The Journal of biological chemistry. 1990;265(34):21355-62. Epub 1990/12/05. PubMed PMID: 2250029.
39. Lillis AP, Van Duyn LB, Murphy-Ullrich JE, Strickland DK. LDL receptor-related protein 1: unique tissue-specific functions revealed by selective gene knockout studies. Physiol Rev. 2008;88(3):887-918. doi: 10.1152/physrev.00033.2007. PubMed PMID: 18626063; PMCID: PMC2744109.
40. Lillis AP, Mikhailenko I, Strickland DK. Beyond endocytosis: LRP function in cell migration, proliferation and vascular permeability. Journal of Thrombosis and Haemostasis. 2005;3(8):1884-93. doi: 10.1111/j.1538-7836.2005.01371.x.
41. Selvais C, D'Auria L, Tyteca D, Perrot G, Lemoine P, Troeberg L, Dedieu S, Noel A, Nagase H, Henriet P, Courtoy PJ, Marbaix E, Emonard H. Cell cholesterol modulates metalloproteinase-dependent shedding of low-density lipoprotein receptor-related protein-1 (LRP-1) and clearance function. FASEB J. 2011;25(8):2770-81. Epub 2011/04/27. doi: 10.1096/fj.10-169508. PubMed PMID: 21518850; PMCID: PMC3470721.
42. Kanekiyo T, Cirrito JR, Liu CC, Shinohara M, Li J, Schuler DR, Shinohara M, Holtzman DM, Bu G. Neuronal clearance of amyloid-beta by endocytic receptor LRP1. J Neurosci. 2013;33(49):19276-83. Epub 2013/12/07. doi: 10.1523/JNEUROSCI.3487-13.2013. PubMed PMID: 24305823; PMCID: PMC3850043.
43. Beisiegel U, Weber W, Ihrke G, Herz J, Stanley KK. The LDL-receptor-related protein, LRP, is an apolipoprotein E-binding protein. Nature. 1989;341(6238):162-4. Epub 1989/09/14. doi: 10.1038/341162a0. PubMed PMID: 2779654.
44. Beisiegel U, Weber W, Bengtsson-Olivecrona G. Lipoprotein lipase enhances the binding of chylomicrons to low density lipoprotein receptor-related protein. Proceedings of the National Academy of Sciences. 1991;88(19):8342.
45. Saenko EL, Yakhyaev AV, Mikhailenko I, Strickland DK, Sarafanov AG. Role of the low density lipoprotein-related protein receptor in mediation of factor VIII catabolism. The Journal of biological chemistry. 1999;274(53):37685-92. Epub 1999/12/23. PubMed PMID: 10608826.
46. Lenting PJ, CJ VANS, Denis CV. Clearance mechanisms of von Willebrand factor and factor VIII. J Thromb Haemost. 2007;5(7):1353-60. Epub 2007/04/12. doi: 10.1111/j.1538-7836.2007.02572.x. PubMed PMID: 17425686.

47. Li Y, Marzolo MP, van Kerkhof P, Strous GJ, Bu G. The YXXL motif, but not the two NPXY motifs, serves as the dominant endocytosis signal for low density lipoprotein receptor-related protein. The Journal of biological chemistry. 2000;275(22):17187-94. Epub 2000/04/05. doi: 10.1074/jbc.M000490200. PubMed PMID: 10747918.
48. Craig J, Mikhailenko I, Noyes N, Migliorini M, Strickland DK. The LDL receptor-related protein 1 (LRP1) regulates the PDGF signaling pathway by binding the protein phosphatase SHP-2 and modulating SHP-2- mediated PDGF signaling events. PloS one. 2013;8(7):e70432. Epub 2013/08/08. doi: 10.1371/journal.pone.0070432. PubMed PMID: 23922991; PMCID: PMC3724782.
49. Boucher P, Li WP, Matz RL, Takayama Y, Auwerx J, Anderson RG, Herz J. LRP1 functions as an atheroprotective integrator of TGFbeta and PDFG signals in the vascular wall: implications for Marfan syndrome. PloS one. 2007;2(5):e448. Epub 2007/05/17. doi: 10.1371/journal.pone.0000448. PubMed PMID: 17505534; PMCID: PMC1864997.
50. Pietrzik CU, Yoon I-S, Jaeger S, Busse T, Weggen S, Koo EH. FE65 Constitutes the Functional Link between the Low-Density Lipoprotein Receptor-Related Protein and the Amyloid Precursor Protein. The Journal of Neuroscience. 2004;24(17):4259-65. doi: 10.1523/jneurosci.5451-03.2004.
51. Betts GN, van der Geer P, Komives EA. Structural and functional consequences of tyrosine phosphorylation in the LRP1 cytoplasmic domain. The Journal of biological chemistry. 2008;283(23):15656-64. doi: 10.1074/jbc.M709514200. PubMed PMID: 18381291; PMCID: PMC2414285.
52. Klug W, Dietl A, Simon B, Sinning I, Wild K. Phosphorylation of LRP1 regulates the interaction with Fe65. FEBS Lett. 2011;585(20):3229-35. doi: 10.1016/j.febslet.2011.09.028. PubMed PMID: 21968187.
53. Guttman M, Betts GN, Barnes H, Ghassemian M, van der Geer P, Komives EA. Interactions of the NPXY microdomains of the low density lipoprotein receptor-related protein 1. Proteomics. 2009;9(22):5016-28. doi: 10.1002/pmic.200900457. PubMed PMID: 19771558; PMCID: PMC2862490.
54. Ranganathan S, Liu CX, Migliorini MM, Von Arnim CA, Peltan ID, Mikhailenko I, Hyman BT, Strickland DK. Serine and threonine phosphorylation of the low density lipoprotein receptor-related protein by protein kinase Calpha regulates endocytosis and association with adaptor molecules. The Journal of biological chemistry. 2004;279(39):40536-44. Epub 2004/07/24. doi: 10.1074/jbc.M407592200. PubMed PMID: 15272003.
55. May P, Bock HH, Nimpf J, Herz J. Differential glycosylation regulates processing of lipoprotein receptors by gamma-secretase. The Journal of biological chemistry. 2003;278(39):37386-92. Epub 2003/07/23. doi: 10.1074/jbc.M305858200. PubMed PMID: 12871934.
56. Goldstein JL, Basu SK, Brown MS. [19] Receptor-mediated endocytosis of low-density lipoprotein in cultured cells. Methods in Enzymology: Academic Press; 1983. p. 241-60.
57. Herz J, Hamann U, Rogne S, Myklebost O, Gausepohl H, Stanley KK. Surface location and high affinity for calcium of a 500-kd liver membrane protein closely related

to the LDL-receptor suggest a physiological role as lipoprotein receptor. EMBO J. 1988;7(13):4119-27. Epub 1988/12/20. PubMed PMID: 3266596; PMCID: PMC455121.
58. Lin H-T, Steller MA, Aish L, Hanada T, Chishti AH. Differential expression of human Dlg in cervical intraepithelial neoplasias. Gynecologic Oncology. 2004;93(2):422-8. doi: https://doi.org/10.1016/j.ygyno.2004.01.025.
59. Shi J, Gilbert GE. Lactadherin inhibits enzyme complexes of blood coagulation by competing for phospholipid-binding sites. Blood. 2003;101(7):2628-36. Epub 2003/01/09. doi: 10.1182/blood-2002-07-1951. PubMed PMID: 12517809.
60. Gilbert GE, Novakovic VA, Shi J, Rasmussen J, Pipe SW. Platelet binding sites for factor VIII in relation to fibrin and phosphatidylserine. Blood. 2015;126(10):1237-44. doi: 10.1182/blood-2015-01-620245. PubMed PMID: 26162408; PMCID: PMC4559935.
61. Faust JR, Goldstein JL, Brown MS. Receptor-mediated uptake of low density lipoprotein and utilization of its cholesterol for steroid synthesis in cultured mouse adrenal cells. Journal of Biological Chemistry. 1977;252(14):4861-71.
62. Huang GN, Zeng W, Kim JY, Yuan JP, Han L, Muallem S, Worley PF. STIM1 carboxyl-terminus activates native SOC, I(crac) and TRPC1 channels. Nat Cell Biol. 2006;8(9):1003-10. Epub 2006/08/15. doi: 10.1038/ncb1454. PubMed PMID: 16906149.
63. Iizuka-Kogo A, Shimomura A, Senda T. Colocalization of APC and DLG at the tips of cellular protrusions in cultured epithelial cells and its dependency on cytoskeletons. Histochem Cell Biol. 2005;123(1):67-73. Epub 2004/12/21. doi: 10.1007/s00418-004-0729-2. PubMed PMID: 15609045.
64. Fanning AS, Anderson JM. Protein–protein interactions: PDZ domain networks. Current Biology. 1996;6(11):1385-8. doi: https://doi.org/10.1016/S0960-9822(96)00737-3.
65. Lee H-J, Zheng JJ. PDZ domains and their binding partners: structure, specificity, and modification. Cell Communication and Signaling : CCS. 2010;8:8-. doi: 10.1186/1478-811X-8-8. PubMed PMID: PMC2891790.
66. Anthis NJ, Haling JR, Oxley CL, Memo M, Wegener KL, Lim CJ, Ginsberg MH, Campbell ID. Beta integrin tyrosine phosphorylation is a conserved mechanism for regulating talin-induced integrin activation. The Journal of biological chemistry. 2009;284(52):36700-10. Epub 2009/10/22. doi: 10.1074/jbc.M109.061275. PubMed PMID: 19843520; PMCID: PMC2794784.